

AD-A142 991

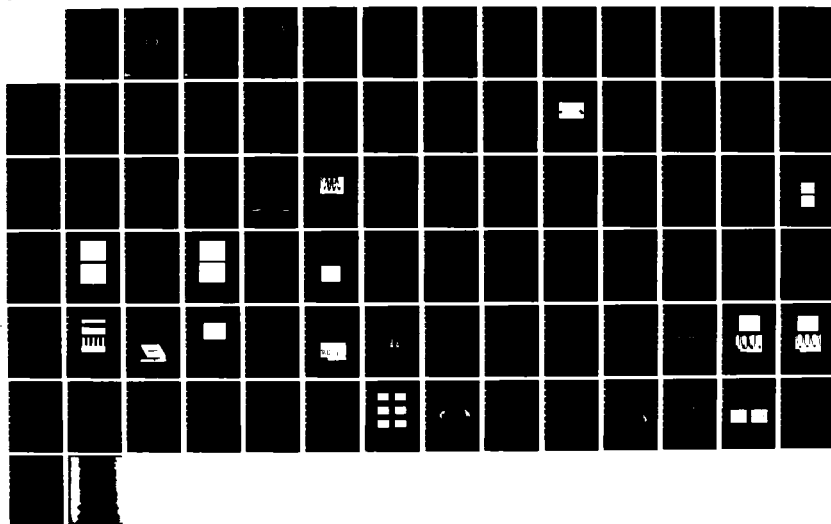
SOLID STATE RESEARCH(U) MASSACHUSETTS INST OF TECH
LEXINGTON LINCOLN LAB A L MCWHORTER 15 NOV 83 1983-4
ESD-TR-83-223

1/1

UNCLASSIFIED

F/G 28/12

NL





MICROCOPY RESOLUTION TEST CHART
NATIONAL BUREAU OF STANDARDS-1963-A

AD-A142 991

Quarterly Technical Report

Solid State Research

DTIC
JUL 13 1984
H

1983:4

Lincoln Laboratory

MASSACHUSETTS INSTITUTE OF TECHNOLOGY

LEXINGTON, MASSACHUSETTS



Prepared under Electronic Systems Division Contract F19628-80-C-0002.

Approved for public release; distribution unlimited.

AIR FORCE APRIL 2, 1984--620

84 07 10 066

The work reported in this document was performed at Lincoln Laboratory, a center for research operated by Massachusetts Institute of Technology, with the support of the Department of the Air Force under Contract F19628-80-C-0002.

This report may be reproduced to satisfy needs of U.S. Government agencies.

The views and conclusions contained in this document are those of the contractor and should not be interpreted as necessarily representing the official policies, either expressed or implied, of the United States Government.

The Public Affairs Office has reviewed this report, and it is releasable to the National Technical Information Service, where it will be available to the general public, including foreign nationals.

This technical report has been reviewed and is approved for publication.

FOR THE COMMANDER

A handwritten signature in dark ink, reading "Thomas J. Alpert". The signature is fluid and cursive, with the first name "Thomas" and last name "Alpert" clearly legible.

Thomas J. Alpert, Major, USAF
Chief, ESD Lincoln Laboratory Project Office

Non-Lincoln Recipients

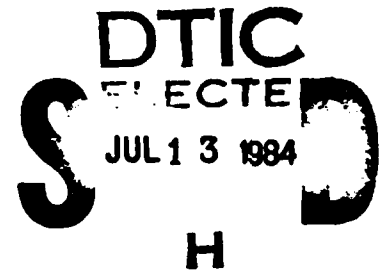
PLEASE DO NOT RETURN

Permission is given to destroy this document
when it is no longer needed.

MASSACHUSETTS INSTITUTE OF TECHNOLOGY
LINCOLN LABORATORY

SOLID STATE RESEARCH

QUARTERLY TECHNICAL REPORT



1 AUGUST — 31 OCTOBER 1983

ISSUED 7 MARCH 1984



Accession For	
NTIS GRA&I	<input checked="" type="checkbox"/>
DTIC TAB	<input type="checkbox"/>
Unannounced	<input type="checkbox"/>
Justification	
By _____	
Distribution/	
Availability Codes	
Dist	Avail and/or Special
A-1	

Approved for public release; distribution unlimited.

LEXINGTON

MASSACHUSETTS

ABSTRACT

This report covers in detail the solid state research work of the Solid State Division at Lincoln Laboratory for the period 1 August through 31 October 1983. The topics covered are Solid State Device Research, Quantum Electronics, Materials Research, Microelectronics, and Analog Device Technology. Funding is primarily provided by the Air Force, with additional support provided by the Army, DARPA, Navy, NASA, and DOE.

TABLE OF CONTENTS

Abstract	iii
List of Illustrations	vii
List of Tables	x
Introduction	xi
Reports on Solid State Research	xiii
Organization	xxi
 1. SOLID STATE DEVICE RESEARCH	 1
1.1 Theory of Voltage and Current Distributions in Mass-Transported GaInAsP InP Buried-Heterostructure Lasers	1
1.2 Linear Light-Current Characteristics in Mass-Transported GaInAsP InP Buried-Heterostructure Lasers	7
1.3 Four-Element 10.6- μ m Photomixer Arrays Operating at 195 K	11
 2. QUANTUM ELECTRONICS	 15
2.1 Analytical Comparison of Optimized Heterodyne and Direct-Detection LIDAR for Atmospheric Remote Sensing	15
2.2 Surface-Photoacoustic-Wave Spectroscopy	18
2.3 Laser Microchemical Techniques for Reversible Restructuring of Gate-Array Prototype Circuits	23
 3. MATERIALS RESEARCH	 29
3.1 Efficient AlGaAs Shallow-Homojunction Solar Cells	29
 4. MICROELECTRONICS	 35
4.1 Fabrication of Etched-Geometry GaAs Permeable-Base Transistors	35
4.2 Nitrocellulose as a Self-Developing Resist with Submicrometer Resolution and Processing Stability	39
4.3 Effect of Base Geometry on Si PBT Device Performance	44
 5. ANALOG DEVICE TECHNOLOGY	 53
5.1 Gaussian Convolution of Images Stored in a Charge-Coupled Device	53
5.2 Superconductive Pulse Compressor	59

LIST OF ILLUSTRATIONS

Figure No.		Page
1-1	SEM Cross-Sectional View of a Laser Mesa Showing the Formation of InP pn Homojunctions in the Transported Regions. Steps Seen in the Transported Regions Are Due to the Straining Procedure Which Preferentially Eroded n-InP, as Confirmed by Rotating the Sample During the SEM Examination	1
1-2	The Schwarz-Christoffel Transformation Used to Obtain the Potential $\Phi(u,v)$ in the Laser Mesa. Dashed Curves Are the Streamlines	2
1-3	Calculated Voltage Distribution for Two Laser Mesas with Different Active Region Widths. Equipotentials Are Separated by Equal Voltage Increments; Numbers Are in Volts. Dashed Curves Are the Streamlines	4
1-4	Sublinear L-I Characteristics Resulting from Adding the Homojunction Current to a Linear One. Calculation of the Homojunction Current Was Carried Out for the Device Geometry Shown in the Insert and for Three Different p-Doping Concentrations. Note That the Numerical Values of the Curve of $p = 4 \times 10^{17} \text{ cm}^{-3}$ Are Listed in Table 1-1	6
1-5	Calculated I_1 as a Function of the Cap p-Doping	8
1-6	L-I Characteristics of Five Mass-Transported BH Lasers with Different Cap-Layer Doping Concentrations. These Devices Were Mounted p-Side Down	9
1-7	Far-Field Patterns in the Junction Plane of a Mass-Transported BH Laser	10
1-8	Photograph of a Linear Array of p-Type HgCdTe Photoconductors Designed for 10.6- μm Heterodyne Operation at 195 K	11
2-1	Predicted Percentage Measurement Error, σ_n , as a Function of Range for the Baseline LIDAR Systems	18
2-2	Linearity of SAW Signal vs Laser Energy for 530-nm Irradiation of a 200-nm-Thick Au Film. The Solid Line Has Unity Slope	19
2-3	Output of EBT with Multiple Spot Illumination. (Top) Through 3- \times 4-mm Shaping Aperture and 50- μm -Period Cr Mask; (Bottom) Cr Mask Removed	20

Figure No.		Page
2-4	SEMs of a Portion of a Ring Oscillator (a) Before and (b) After Laser-Microchemical Restructuring. One Short Vertical Al Link Has Been Removed, and One Long Horizontal Poly-Si Link Has Been Added	22
2-5	SEMs of Doped Poly-Si Lines Deposited Using Laser Microchemistry onto Gate-Array Chip. Showing (a) Step Coverage and (b) Formation of Contact with Al. The Bars in (a) and (b) Indicate 1- and 10- μ m Lengths, Respectively	24
2-6	Electrical Characteristics of Ring Oscillator Circuits. (a) Oscillator Period vs Supply Voltage for a Ring Oscillator Before and After Restructuring from 23 to 19 Stages; (b) Oscillator Waveform of a 19-Stage Restructured Oscillator	26
3-1	Schematic Cross Section of AlGaAs Shallow-Homojunction Solar Cell	30
3-2	Current Density as a Function of Voltage under Simulated AM1 Conditions for $\text{Al}_{0.2}\text{Ga}_{0.8}\text{As}$ Cell with 12.9 Percent Conversion Efficiency	31
3-3	Short-Circuit Current Density J_{sc} as a Function of Open-Circuit Voltage V_{oc} at Different Illumination Levels for the Cell of Figure 3-2	32
3-4	External Quantum Efficiency as a Function of Wavelength for the Cell of Figure 3-2	33
4-1	Fabrication Sequence for Etched-Geometry GaAs PBTs	36
4-2	SEMs of the Etched GaAs Grating Which Forms the Device Active Region	37
4-3	Schematic Diagram of an Etched-Geometry GaAs PBT	38
4-4	SEM of a Completed Etched-Geometry GaAs PBT	38
4-5	Typical Three-Terminal Current-Voltage Characteristics of an Etched-Geometry GaAs PBT. The Top Trace Is at a +0.6-V Base-to-Emitter Bias and the Steps Are 0.2 V	39
4-6	Etch Rate of Nitrocellulose as a Function of Ar^+ Energy Minus a Threshold Energy of 50 eV. The Data Are Normalized to a Beam Current of 1 mA cm^{-2} . The Sputtering Rates of Tantalum and Copper, Obtained from the Data of References 12 and 13, Are Shown for Comparison	40

Figure No.		Page
4-7	SEM of a Grating Pattern in a 0.6- μm -Thick Nitrocellulose Film on a Silicon Wafer. The Sample Was Exposed to a Beam of 500-eV Ar^+ at a Current Density of 0.25 mA cm^{-2} for 40 s. The SiN_x Stencil Mask Used for this Exposure Consisted of a 320-nm Grating with a Crossmember Every 3.8 μm to Strengthen the Mask. Two Shadows of the Crossmembers Can Be Seen in the Nitrocellulose	41
4-8	Volatile Decomposition Products of Nitrocellulose When Exposed to a Beam of 2-keV Xe^+ at 1 mA cm^{-2} . The Products Were Detected by a Quadrupole Mass Spectrometer and the Background Gas Spectrum Was Subtracted from the Data	42
4-9	Reactive-Ion Etching Rate of Nitrocellulose, SiO_2 , and Ferrocene-Doped Nitrocellulose. The Etch Gas Was CHF_3 at a Pressure of 25 Torr and a Flow Rate of 45 sccm. The Samples Were Placed on a Quartz Plate Which Covered the Water-Cooled Powered Electrode	43
4-10	Comparison of Three Base Geometry Configurations for the Si PBT. The Differences Are in the Metal-Semiconductor Contact Area in the Base Region	44
4-11	Comparison of J_c vs V_{BE} for the Overgrown Si PBT, the Etched Collector Structure With Sidewall Contact, and the Etched Collector Structure Without Sidewall Contact at $V_{CE} = 1.0 \text{ V}$. L Is Base Metal Thickness and d Is Spacing Between Adjacent Base Finders	45
4-12	Unity Short-Circuit Current-Gain Frequency, f_T , as a Function of V_{BE} for the Same Devices as Figure 4-11	46
4-13	Comparison of Important Parameters for the Three Device Configurations Described in Figures 4-10 Through 4-12	47
4-14	SEM of the Base Region of a Si PBT, Where the W Base Metal Is Separated from the Si Sidewall. In the Corresponding I-V Characteristics Shown Above, $V_{BE} = +0.4$ for the Top Curve	48
4-15	SEM of the Base Region of a Si PBT in Which the Base Metal Appears To Be in Partial Contact with the Si Sidewall. In the Corresponding I-V Characteristics Shown Above, $V_{BE} = +0.4$ for the Top Curve	49
5-1	Example of a CCD Structure in Which Gaussian Convolution Can Be Carried Out	54

Figure No.		Page
5-2	Clocking Waveforms Used to Produce Gaussian Convolution of a Signal Stored in a CCD. The A-I Designations of Time Are Keyed to the Charge Mixing Sequence in Figure 5-3	54
5-3	Potential Wells and Charge Packets in a Standard Four-Phase CCD Clocked with the Waveforms Shown in Figure 5-2. Two Mixing Cycles Are Shown Here	55
5-4	Photographs of the Results Obtained with a 32-Stage Four-Phase CCD with 1, 2, 4, 8, and 16 Mixing Cycles Applied to an Initial Pattern of Eight Full Wells	57
5-5	Insertion Loss vs Frequency of a Hamming-Weighted Superconductive Chirp Filter	58
5-6	Phase Error (Deviation from Quadratic) of a Hamming-Weighted Superconductive Chirp Filter	60
5-7	Insertion Loss vs Frequency of a Flat-Weighted Superconductive Chirp Filter	61
5-8	Phase Error (Deviation from Quadratic) of a Flat-Weighted Superconductive Chirp Filter	62
5-9	(a) Compressed Pulse Response of Matched Flat- and Hamming-Weighted Superconductive Chirp Filters and (b) Same with 26 dB More Gain	63

LIST OF TABLES

Table No.		Page
1-1	Calculated I_H and Related Parameters as a Function of I_Q for $p = 4 \times 10^{17} \text{ cm}^{-3}$, $a = 5.0 \text{ } \mu\text{m}$, $W = 1.5 \text{ } \mu\text{m}$, and $b = 2.0 \text{ } \mu\text{m}$	5
1-2	4-Element Photomixer Array Performance at 195 K	12
2-1	List of Parameter Values for the Two Baseline DIAL Systems	17
5-1	Comparisons for 1, 2, 4, and 8 Mixing Cycles of the Charge Packet Values Measured, the Values Expected for an Idealized CCD, and the Values for True Gaussian Convolution	56

INTRODUCTION

1. SOLID STATE DEVICE RESEARCH

A technique has been developed to calculate the voltage and current distributions in the mass-transported GaInAsP/InP buried-heterostructure lasers. It is valuable for designing lasers for operation without current leakage through the InP pn homojunctions formed in the transported regions.

Mass-transported GaInAsP/InP buried-heterostructure lasers with low threshold currents and a linear light output to greater than 13 mW per facet have been obtained. This is achieved by using sufficient p-doping in the cap layer of the starting double-heterostructure wafer.

Uniform 4-element linear arrays of 250-MHz bandwidth 10.6- μ m HgCdTe photomixers have been developed with an average NEP of 3.5×10^{-19} W/Hz at 195 K and a cooling requirement that is compatible with standard 4-stage thermoelectric coolers.

2. QUANTUM ELECTRONICS

An analytical comparison has been made of an optimized heterodyne and a direct-detection CO₂ LIDAR for atmospheric remote sensing. The results predict that significant improvement may be obtained through further progress in the development of direct detectors.

The sensitivity of laser surface photoacoustic wave spectroscopy has been improved to an absorbance of 2×10^{-8} of the laser energy by the use of lower center frequency surface-acoustic-wave (SAW) transducers which are a better match to the acoustic frequencies generated by the focused light. An additional improvement involves the use of multiple spot imaging through a Cr mask, allowing increased laser energy without increasing laser fluence.

Laser direct-write Al etching and poly-Si deposition have been adapted to the mask-free alteration of simple gate-array test circuits on CMOS chips. These new methods may be useful for rapid evaluation and optimization of integrated-circuit prototypes.

3. MATERIALS RESEARCH

As a first step in the development of AlGaAs-Si tandem solar cells, shallow-homojunction cells have been fabricated in Al_{0.2}Ga_{0.8}As epitaxial layers grown on single-crystal GaAs substrates by organometallic chemical-vapor deposition. The one-sun conversion efficiency measured for the best cell was 12.9 percent at AM1.

Epitaxial layers of GaAs and Al_xGa_{1-x}As ($0.2 \leq x \leq 0.5$) have been grown directly on single-crystal Si(100) substrates, without an intermediate Ge layer, by molecular beam epitaxy (MBE). To improve nucleation, after being chemically cleaned the substrates were preheated in the MBE system at $\sim 800^\circ\text{C}$ to reduce surface contamination and achieve ordered surface reconstruction prior to growth.

4. MICROELECTRONICS

Etched-geometry GaAs permeable-base transistors (PBTs) have been fabricated and tested. These differ from previously reported PBTs in that the base metal is not encapsulated in GaAs, thus avoiding difficult overgrowth processes. A small-signal, unity-current-gain frequency f_T of 13 GHz has been measured for initial devices. Improvements in device fabrication should yield an $f_T > 40$ GHz.

Nitrocellulose has been demonstrated to be a self-developing resist with submicrometer resolution. Simultaneous exposure and development were accomplished by irradiation with low-energy Ar^+ or Xe^+ , and by exposure to UV light.

The effect of base metal-semiconductor contact area on Si PBT performance has been investigated. Experimental results and numerical simulations of different configurations show that the intrinsic f_T is invariant with contact area, but that the measured (extrinsic) f_T is optimized by maximizing the contact area.

5. ANALOG DEVICE TECHNOLOGY

A new method for producing the convolution of a Gaussian function with an optical image stored in a charge-coupled device array has been demonstrated. Such Gaussian convolution operations are the time-consuming steps in the difference-of-Gaussians procedure employed in artificial-intelligence algorithms for the detection and localization of the edges of objects in an image. This method has the potential of producing such convolutions in two dimensions for arbitrarily large fields of view in a time less than that required to detect the original image.

Pulse compression has been demonstrated with a matched pair of superconductive chirp filters. The tapped-delay-line filters, consisting of niobium superconductor and silicon dielectric in a stripline structure, have a bandwidth of 2.3 GHz and 17.5 ns of dispersion and are amplitude-weighted for flat and Hamming responses. Phase errors of less than 10° rms and relative sidelobe levels of -25 dB have been achieved.

REPORTS ON SOLID STATE RESEARCH

15 September through 15 November 1983

PUBLISHED REPORTS

Journal Articles

JA No.

- | | | | |
|------|---|---|---|
| 5397 | Multigigahertz-Bandwidth Linear-Frequency-Modulated Filters Using a Superconductive Stripline | J.T. Lynch
R.S. Withers
A.C. Anderson
P.V. Wright
S.A. Reible | Appl. Phys. Lett. 43 ,
319 (1983) |
| 5419 | The Mechanism of Orientation in Si Graphoepitaxy by Laser or Strip-Heater Recrystallization | H.I. Smith*
C.V. Thompson*
M.W. Geis
R.A. Lemons*
M.A. Bosch* | J. Electrochem. Soc. 130 ,
2050 (1983) |
| 5445 | Fourier Transformation Using an Electroabsorptive CCD Spatial Light Modulator | R.H. Kingston
F.J. Leonberger | IEEE J. Quantum Electron.
QE-19 , 1443 (1983) |
| 5449 | Broadly Tunable Modelocked HgCdTe Lasers | R.S. Putnam*
M.M. Salour*
T.C. Harman | Appl. Phys. Lett. 43 ,
408 (1983) |
| 5466 | Enhanced Raman Scattering from Silicon Microstructures | D.V. Murphy
S.R.J. Brueck | Opt. Lett. 8 , 494 (1983) |
| 5474 | Effect of Magnetic Transition on the H-D Exchange Reaction on $\text{Ni}_{1-x}\text{Cu}_x$ Alloys | H.J. Zeiger
B. Wasserman*
M.S. Dresselhaus*
G. Dresselhaus* | Phys. Rev. B 28 , 317
(1983) |
| 5481 | Assessment of Relative Error Sources in IR DIAL Measurement Accuracy | N. Menyuk
D.K. Killinger | Appl. Opt. 22 , 2690 (1983) |

* Author not at Lincoln Laboratory.

JA No.

- | | | | |
|------|---|---|--|
| 5490 | Fully Isolated Lateral Bipolar — MOS Transistors Fabricated in Zone-Melting-Recrystallized Si Films on SiO ₂ | B-Y. Tsaur
D.J. Silversmith
J.C.C. Fan
R.W. Mountain | IEEE Electron Device Lett. EDL-4 , 269 (1983) |
| 5494 | Resonant Tunneling Through Quantum Wells at Frequencies Up to 2.5 THz | T.C.L. Gerhard
W.D. Goodhue
P.E. Tannenwald
C.D. Parker
D.D. Peck | Appl. Phys. Lett. 43 , 588 (1983) |
| 5503 | Optical Heterodyne Spectroscopy with Frequency-Modulated and Amplitude-Modulated Semiconductor Lasers | W. Lenth | Opt. Lett. 8 , 575 (1983) |
| 5509 | Optimal Design of Amorphous Single-Junction and Tandem Solar Cells | J.C.C. Fan
B.J. Palm | Solar Cells 10 , 81 (1983) |

Meeting Speeches**MS No.**

- | | | | |
|-------|--|---|---|
| 6008B | High-Efficiency Crystalline Tandem Cells | J.C.C. Fan
B-Y. Tsaur
B.J. Palm | <i>Photovoltaics for Solar Energy Applications II</i> , D. Adler, Ed., Proc. SPIE 407 , 73-87 (1983) |
| 6033 | Heterodyne and Direct Detection at 10 μ m with High-Temperature p-Type HgCdTe Photodetectors | D.L. Spears | Proc. Mtg. of IRIS Specialty Group on Infrared Detectors, San Diego, California, 27-29 July 1982, Vol. I, pp. 163-177 |
| 6073 | Electronic Properties of Grain Boundaries in GaAs: A Study of Oriented Bicrystals Prepared by Epitaxial Lateral Overgrowth | J.P. Salerno
R.W. McClelland
J.G. Mavroides
J.C.C. Fan
A.F. Witt* | <i>Materials Research Society Symposium Proceedings, Vol. 14</i> (Elsevier, New York, 1983), pp. 375-382 |

* Author not at Lincoln Laboratory.

MS No.

- | | | | |
|-------|--|---|---|
| 6192A | Advances in LEC Growth of InP Crystals | G.W. Iseler | Proc. 2nd NATO Workshop on Materials Aspects of InP, Lancaster, U.K., 28-30 March 1983, pp. 10-1 — 10-6 |
| 6271 | Monolithic Frequency Doublers | A. Chu
W.E. Courtney
L.J. Mahoney
R.A. Murphy
R.W. McClelland | <i>IEEE 1983 Microwave and Millimeter-Wave Monolithic Circuits Symposium</i> , Digest of Papers, B.E. Spielman, Ed. (IEEE, New York, 1983), pp. 45-49 |

* * * * *

UNPUBLISHED REPORTS**Journal Articles****JA No.**

- | | | | |
|------|---|--|--|
| 5480 | Dual Ion Implantation Technique for Formation of Shallow p ⁺ /n Junctions in Silicon | B-Y. Tsaur
C.H. Anderson, Jr. | Accepted by J. Appl. Phys. |
| 5482 | A Technique for the Determination of Stress in Thin Films | E.I. Bromley
J.N. Randall
D.C. Flanders
R.W. Mountain | Accepted by J. Vac. Sci. Technol. |
| 5495 | Use of Plasma-Deposited Si ₃ N ₄ as an Oxidation Mask in the Fabrication of GaAs Shallow-Homojunction Solar Cells | G.W. Turner
M.K. Connors | Accepted by J. Electrochem. Soc. |
| 5496 | Self-Developing UV Photoresist Using Excimer Laser Exposure | T.F. Deutsch
M.W. Geis | Accepted by Appl. Phys. Lett. |
| 5499 | A CCD Time-Integrating Correlator | B.E. Burke
D.L. Smythe | Accepted by IEEE J. Solid-State Circuits |
| 5500 | A Review of Laser-Microchemical Processing | D.J. Ehrlich
J.Y. Tsao | Accepted by J. Vac. Sci. Technol. |
| 5504 | A High-Speed Digitally Programmable CCD Transversal Filter | A.M. Chiang
B.E. Burke | Accepted by IEEE J. Solid-State Circuits |

JA No.

- | | | | |
|------|---|--|-----------------------------------|
| 5508 | Orientation Filtering by Growth-Velocity Competition in Zone-Melting Recrystallization of Silicon on SiO ₂ | H.A. Atwater*
C.V. Thompson*
H.I. Smith*
M.W. Geis | Accepted by Appl. Phys. Lett. |
| 5512 | Effects of Dry Etching on GaAs | S.W. Pang
G.A. Lincoln
R.W. McClelland
P.D. DeGraff
M.W. Geis
W.J. Piacentini | Accepted by J. Vac. Sci. Technol. |
| 5513 | Read-Only Memory with Electron-Beam Programmable Floating-Gate Transistors | D.C. Shaver | Accepted by J. Vac. Sci. Technol. |
| 5515 | Silicon Nitride Stencil Masks for High Resolution Ion Lithography Proximity Printing | J.N. Randall
D.C. Flanders
N.P. Economou
J.P. Donnelly
E.I. Bromley | Accepted by J. Vac. Sci. Technol. |
| 5517 | Nitrocellulose as a Self-Developing Resist with Sub-micrometer Resolution and Processing Stability | M.W. Geis
J.N. Randall
T.F. Deutsch
N.N. Efremow
J.P. Donnelly
J.D. Woodhouse | Accepted by J. Vac. Sci. Technol. |
| 5520 | Large Area Ion Beam Assisted Etching of GaAs with High Etch Rates and Controlled Anisotropy | G.A. Lincoln
M.W. Geis
S.W. Pang
N.N. Efremow | Accepted by J. Vac. Sci. Technol. |
| 5527 | Zone Melting Recrystallization of Thick Silicon on Insulator Films | H.A. Atwater*
H.I. Smith*
C.V. Thompson*
M.W. Geis | Accepted by Mater. Lett. |
| 5528 | Optimal Design of Amorphous/Crystalline Tandem Cells | J.C.C. Fan
B.J. Palm | Accepted by Solar Cells |

* Author not at Lincoln Laboratory.

JA No.

- | | | | |
|------|--|--|---|
| 5534 | Structural Characterization by Transmission Electron Emission Microscopy of Silicon Grown Over Submicrometer-Period Gratings of Deposited Tungsten | B.A. Vojak
D.D. Rathman
J.A. Burns
S.M. Cabral
N.N. Efremow | Accepted by Appl. Phys. Lett. |
| 5536 | Monolithic Silicon Bolometers | P.M. Downey*
A.D. Jeffries*
S.S. Meyer*
R.W. Weiss*
F.J. Bachner
J.P. Donnelly
W.T. Lindley
R.W. Mountain
D.J. Silversmith | Accepted by Appl. Opt. |
| 5549 | Dry Etching Induced Damage in Si and GaAs | S.W. Pang | Accepted by Solid State Technol. |
| 5552 | Frequency Modulation (FM) Spectroscopy: Theory of Lineshapes and Signal-to-Noise Analysis | G.C. Bjorklund*
M.D. Levenson*
W. Lenth
C. Ortiz* | Accepted by Appl. Phys. B |
| 5556 | Laser Microchemical Processing: Spatial Resolution and Rate Limits of Optical Direct-Writing Techniques | D.J. Ehrlich
J.Y. Tsao | Accepted as Book Chapter (Academic Press, Orlando, Florida) |

Meeting Speeches[†]**MS No.**

- | | | | |
|-------|---|--|---|
| 5707K | Laser Direct-Writing of Microstructures | D.J. Ehrlich | Seminar, Bell Laboratories, Murray Hill, New Jersey, 8 September 1983 |
| 6078B | Excitation of Surface Optical Waves and Material Ripples by Stimulated Scattering | S.R.J. Brueck
D.J. Ehrlich
J.Y. Tsao | Seminar, Columbia University, New York, 26 October 1983 |

* Author not at Lincoln Laboratory.

[†] Titles of Meeting Speeches are listed for information only. No copies are available for distribution.

MS No.

6082C	Zone Melting Recrystallization of Semiconductor Films	M.W. Geis H.I. Smith* B-Y. Tsaur J.C.C. Fan D.J. Silversmith R.W. Mountain R.L. Chapman	SOI Seminar, Palo Alto, California, 31 October 1983
6147B	Spectral Properties of Tunable Lasers	A. Mooradian	International Laser Conference, Canton, China, 6-9 September 1983
6222A	Enhanced Raman Scattering from Crystalline Si Due to Submicrometer Roughness	D.V. Murphy S.R.J. Brueck	Gordon Conference on Non-linear Optics and Lasers, Wolfeboro, New Hampshire, 1-5 August 1983
6405	Mode-Locked Operation of Co:MgF ₂ and Ni:MgF ₂ Lasers	B.C. Johnson P.F. Moulton A. Mooradian	
6227A	New Developments in Mass-Transported GaInAsP/InP Buried-Heterostructure Lasers	Z.L. Liao J.N. Walpole D.Z. Tsang	GTE Laboratories Seminar, Waltham, Massachusetts, 18 August 1983
6255A	Applications of Excimer Lasers to Semiconductor Processing	T.F. Deutsch	Austrian Physical Society Annual Meeting, Linz, Austria, 28-30 September 1983
6307A	Modification of Schottky Diodes Characteristics in GaAs by Dry Etching	S.W. Pang G.A. Lincoln M.W. Geis A. Vera	IEEE Cornell Conference, Ithaca, New York, 15-17 August 1983
6310B	Permeable Base Transistor	R.A. Murphy	Seminar, Raytheon Company, Lexington, Massachusetts, 19 October 1983
6336A	Q-Switched Semiconductor Diode Lasers	D.Z. Tsang J.N. Walpole Z.L. Liao	GTE Laboratories Seminar, Waltham, Massachusetts 14 September 1983
6341	Dual Ion Implantation Technique for Formation of Shallow p ⁺ /n Junctions in Silicon	B-Y. Tsaur C.H. Anderson, Jr. D.J. Silversmith R.W. Mountain	Electrochemical Society Mtg., Washington, DC, 9-14 October 1983

* Author not at Lincoln Laboratory.

MS No.		
6342	PdSi ₂ /Poly-Si Contacts for Si Devices	B-Y. Tsaur
6425	Correction of Metallization Defects on Silicon IC's by Laser Induced Microchemistry	J.Y. Tsao D.J. Ehrlich D.J. Silversmith R.W. Mountain
6361A	Dry Etching-Induced Damage in Si and GaAs	S.W. Pang
6362	Optical Heterodyne Spectroscopy with Frequency and Amplitude Modulated (GaAl)As Diode Lasers	W. Lenth
6365	Laser Remote Sensing and Spectral Identification of Complex Molecules: Current Status and Future Trends	D.K. Killinger N. Menyuk
6372	Optics in Microlithography	N.P. Economou
6373	Gigahertz Optical Analog-to-Digital Converters	R.A. Becker F.J. Leonberger
6375	Comparison of New Analog Device Technologies for Signal Processing	E. Stern
6378	Measurement of Electroacoustic Coefficients in LiNbO ₃ and LiTaO ₃ and Application to Signal-Processing Devices	P. Gottschalk D.E. Oates P.V. Wright
6379	Surface-Photoacoustic-Wave Spectroscopy of Thin Films	D.E. Oates S.R.J. Brueck T.F. Deutsch
6385	Integration of Multiple Elastic Convolver into a Communication Signal Processor	V.S. Dolat G.T. Flynn
6389	Wideband Analog Signal Processing	S.A. Reible R.S. Withers A.C. Anderson J.B. Green
		Electrochemical Society Mtg., Washington, DC, 9-14 October 1983
		Seminar, Martin Marietta Laboratory, Baltimore, Maryland, 17 October 1983
		1983 Annual Meeting of the Optical Society of America, New Orleans, Louisiana, 17-20 October 1983
		1983 Ultrasonics Symposium, Atlanta, Georgia, 31 October — 2 November 1983
		Workshop on Josephson Digital Devices, Circuits and Systems, Lake Tahoe, Nevada, 25-29 September 1983

MS No.

6394	Laser Photochemical Processing	D.J. Ehrlich J.Y. Tsao	Microcircuit Engineering '83, Cambridge, England, 26-29 September 1983
6421	Solar Cell Applications of OMCVD	R.P. Gale	Workshop on OMCVD Growth, Ithaca, New York, 18-19 August 1983
6423	InP Optoelectronic Switches and Their High-Speed Signal-Processing Applications	C.H. Cox III V. Diadiuk F.J. Leonberger R.C. Williamson	27th Annual International SPIE Symposium, San Diego, California, 25 August 1983
6439	Auger Analysis of Electronic Materials — Some Illustrative Examples	M.C. Finn	Society for Applied Spectroscopy, Boston, 14 October 1983
6446	Laser Direct Writing by Surface Microchemistry	J.Y. Tsao D.J. Ehrlich	Seminar, IBM Research Laboratories, San Jose, California, 11 October 1983
6453	Single Chip CCD Signal Processing Devices	A.M. Chiang	Seminar, Analog Devices, Inc., Wilmington, Massachusetts, 13 October 1983
6454	Optimal Design of High-Efficiency Concentrator Space Cells at 80°C and 100 Suns	J.C.C. Fan B.J. Palm	Space Photovoltaic Re- search and Technology Con- ference, Cleveland, Ohio, 19 October 1983

ORGANIZATION

SOLID STATE DIVISION

A.L. McWhorter, *Head*
I. Melngailis, *Associate Head*
E. Stern, *Associate Head*
J.F. Goodwin, *Assistant*

P.E. Tannenwald, *Senior Staff*

QUANTUM ELECTRONICS

A. Mooradian, *Leader*
P.L. Kelley, *Associate Leader*

Barch, W.E.	Johnson, B.C.*
Belanger, L.J.	Killinger, D.K.
Brueck, S.R.J.	Lenth, W.
Burke, J.W.	Menyuk, N.
Bushee, J.F., Jr.	Moulton, P.F.
DeFeo, W.E.	Rosenbluh, M.†
Deutsch, T.F.	Sedlacek, J.H.C
Ehrlich, D.J.	Sharpe, K.A.
Feldman, B.	Sullivan, D.J.
Hancock, R.C.	Tsao, J.Y.
Harrison, J.*	

ELECTRONIC MATERIALS

A.J. Strauss, *Leader*
J.C.C. Fan, *Associate Leader*
J.G. Mavroides, *Senior Staff*
H.J. Zeiger, *Senior Staff*

Anderson, C.H., Jr.	Kolesar, D.F.
Branz, H.M.*	Krohn, L., Jr.
Button, M.J.	Mastromattei, E.L.
Chapman, R.L.	McClelland, R.W.
Chen, C.K.	Metze, G.M.
Choi, H.K.	Nitishin, P.M.
Connors, M.K.	Palm, B.J.
Delaney, E.J.	Pantano, J.V.
Fahey, R.E.	Tracy, D.M.
Finn, M.C.	Tsaur, B-Y.
Gale, R.P.	Turner, G.W.
Iseler, G.W.	Windhorn, T.H.
King, B.D.	

APPLIED PHYSICS

R.C. Williamson, *Leader*
F.J. Leonberger, *Assistant Leader*
T.C. Harman, *Senior Staff*
R.H. Kingston, *Senior Staff*
R.H. Rediker, *Senior Staff*

Becker, R.A.	Hakimi, F.*	Plonko, M.C.
Carter, F.B.	Hovey, D.L.	Schloss, R.P.*
Chinnock, C.B.	Johnson, L.M.	Spears, D.L.
Cox, C.H., III	Liau, Z.L.	Tsang, D.Z.
DeMeo, N.L., Jr.	Lind, T.A.	Walpole, J.N.
Diadiuk, V.	McBride, W.F.	Whitaker, N.*
Donnelly, J.P.	Molter-Orr, L.*	Woodhouse, J.D.
Ferrante, G.A.	O'Donnell, F.J.	Yap, D.*
Groves, S.H.	Paladino, A.E.	

* Research Assistant

† Summer Staff

ANALOG DEVICE TECHNOLOGY

J.H. Cafarella, *Leader*

R.W. Ralston, *Associate Leader*

Anderson, A.C.
Arsenault, D.R.
Boisvert, R.R.
Bouman, C.A.
Brogan, W.T.
Dolat, V.S.
Fischer, J.H.
Fitch, G.L.
Flynn, G.T.

Gottschalk, P.G.*
Green, J.B.
Hauser, E.M.
Holtham, J.H.
Kernan, W.C.
Lattes, A.L.
Leung, I.
Macedo, E.M., Jr.
Macropoulos, W.

Melngailis, J.†
Oates, D.E.
Reible, S.A.
Sage, J.P.
Slattery, R.L.
Withers, R.S.
Yao, I.

MICROELECTRONICS

W.T. Lindley, *Leader*

F.J. Bachner, *Associate Leader*

N.P. Economou, *Assistant Leader*

R.A. Murphy, *Assistant Leader*

Bozler, C.O.
Bromley, E.I.
Burke, B.E.
Cabral, S.M.
Calawa, A.R.
Chen, C.L.
Chiang, A.M.
Chu, A.
Clifton, B.J.
Daniels, P.J.
Durant, G.L.
Efremow, N.N., Jr.
Felton, B.J.
Flanders, D.C.

Geis, M.W.
Gray, R.V.
Hollis, M.A.
Lax, B.†
Lincoln, G.A., Jr.
Lyszcza, T.M.
Mahoney, L.J.
Manfra, M.J.
McGonagle, W.H.
Mountain, R.W.
Mroczkowski, I.H.
Nichols, K.B.
Pang, S.W.
Parker, C.D.

Peck, D.D.
Piacentini, W.J.
Pichler, H.H.
Rabe, S.
Randall, J.N.
Rathman, D.D.
Shaver, D.C.
Silversmith, D.J.
Smythe, D.L., Jr.
Sollner, T.C.L.G.
Taylor, J.A.*
Vera, A.
Vojak, B.A.
Wilde, R.E.

* Research Assistant

† Part Time

1. SOLID STATE DEVICE RESEARCH

1.1 THEORY OF VOLTAGE AND CURRENT DISTRIBUTIONS IN MASS-TRANSPORTED GaInAsP/InP BURIED-HETEROSTRUCTURE LASERS

A technique has been developed to calculate the voltage and current distributions in the mass-transported GaInAsP/InP buried-heterostructure laser. Consider the current flowing from the ohmic contact on top of a laser mesa such as that shown in Figure 1-1. When the

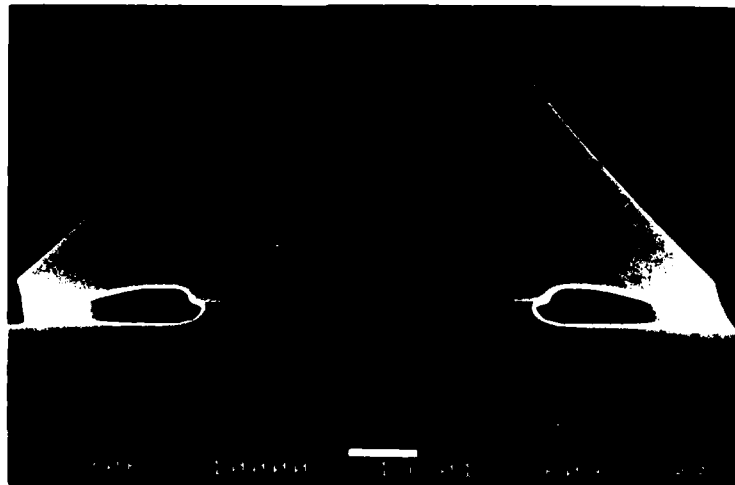


Figure 1-1. SEM cross-sectional view of a laser mesa showing the formation of InP pn homojunctions in the transported regions. Steps seen in the transported regions are due to the staining procedure which preferentially eroded n-InP, as confirmed by rotating the sample during the SEM examination.

current is relatively low, it flows predominantly through the active region with only a negligibly small portion flowing through the InP pn homojunctions, because the quaternary has an energy gap smaller than that of InP. This current-flow pattern and the corresponding voltage distribution in the laser mesa has been analyzed by using a conformal mapping technique, the Schwarz-Christoffel transformation, to be described in this section. The forward-bias voltages along the InP pn homojunctions are obtained from this analysis and can be used to check if the homojunction current indeed remains negligibly small. Thus, the present calculation scheme is valuable in predicting the current limit within which the laser can be operated without leakage through the homojunctions.

As illustrated in Figures 1-2 and -3, the cross section of the laser mesa is approximated as a trapezoidal region with base angles of $\alpha = 0.927$ rad ($= 53^\circ$) in the upper complex w -plane ($w = u + iv$). The active region is approximated as an equipotential line segment (from $w = -W$ to $w = W$). Another equipotential is near the ohmic contact on the

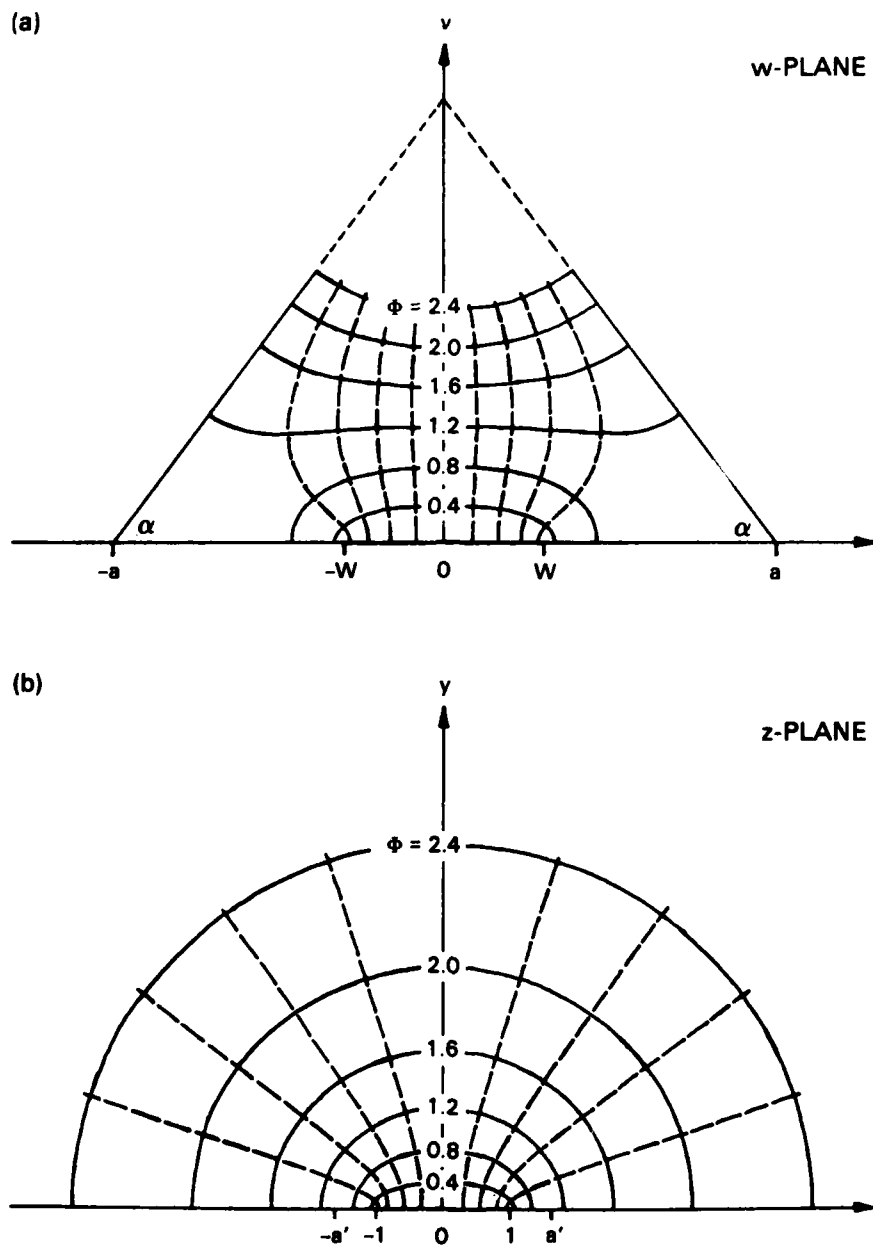


Figure 1-2. The Schwarz-Christoffel transformation used to obtain the potential $\Phi(u,v)$ in the laser mess. Dashed curves are the streamlines.

mesa top. In addition, no current is allowed to flow across the mesa sidewalls and the InP pn homojunctions. These boundary conditions are to be satisfied by the potential $\Phi(u,v)$. The latter is obtained by transforming a known potential $\Phi(x,y)$ from the upper complex z-plane ($z = x + iy$).

The potential $\Phi(x,y)$ in Figure 1-2(b) is that of a two-dimensional current flow from infinity into a slit opening^{1,2} which has a width from $z = -1$ to $z = 1$ and is maintained at a constant potential of $\Phi = 0$. The equipotentials are confocal ellipses, with foci at $z = -1$ and $z = 1$, and are given by

$$\frac{x^2}{\cosh^2 \Phi} + \frac{y^2}{\sinh^2 \Phi} = 1 \quad (1-1)$$

The upper complex z-plane is transformed into the triangular region in the upper complex w-plane in Figure 1-2(a) by^{1,2}

$$w = K \int_0^z (z' + a')^{(\alpha/\pi)-1} (z' - a')^{(\alpha/\pi)-1} dz' \quad (1-2)$$

where K and a' are constants and are determined by requiring the mapping of $z = 1$ and a' to $w = W$ and a , respectively.

By evaluating Equations (1-1) and (1-2) numerically, $\Phi(u,v)$ is obtained. Some examples are shown in Figures 1-2(a) and -3. [The equipotentials in Figure 1-3 are labeled in V which is related to Φ by Equation (1-3) to be discussed below.] Note the equipotentials near the mesa tops are curved, and one of them will approximately coincide with the front of the Zn skin-diffused p^+ region.

The potential $\Phi(u,v)$ is then converted into the voltage distribution $V(u,v)$ by using

$$V(u,v) = \frac{\rho I_Q}{\pi L} \Phi(u,v) + V_Q \quad (1-3)$$

where ρ and L are the resistivity and device length, respectively, and I_Q and V_Q are the current flowing through and the junction voltage at the quaternary region, respectively. Equation (1-3) is obtained by letting $V(u,v) = \text{constant} \times \Phi(u,v) + V_Q$ and by requiring $L/\rho \int_{-W}^W [\partial V/\partial v]_{v=0} du = I_Q$. The junction voltage V_Q is computed to be 0.98 V, by using published values of the band-structure parameters and threshold carrier density.^{3,4}

Figure 1-3 shows examples of calculated $V(u,v)$. In these calculations and others to follow, $L = 300 \mu\text{m}$ and $\rho = (pq \mu_p)^{-1}$ with $\mu_p = 70 \text{ cm}^2/(\text{V}\cdot\text{s})$ were used. The voltage distribution may now be used to estimate the current I_H due to the forward-biased InP homojunctions. The homojunctions are approximated as ideal diodes, and I_H is assumed to be dominated by the electron injection into the p-InP cap region, since the n-InP buffer layer is generally more heavily doped and electrons have considerably higher diffusivity than holes. Therefore,

$$I_H = q \frac{A_H D_n}{L_n} \frac{n_i^2}{p} \exp \left[\frac{qV_H}{kT} \right] \quad (1-4)$$

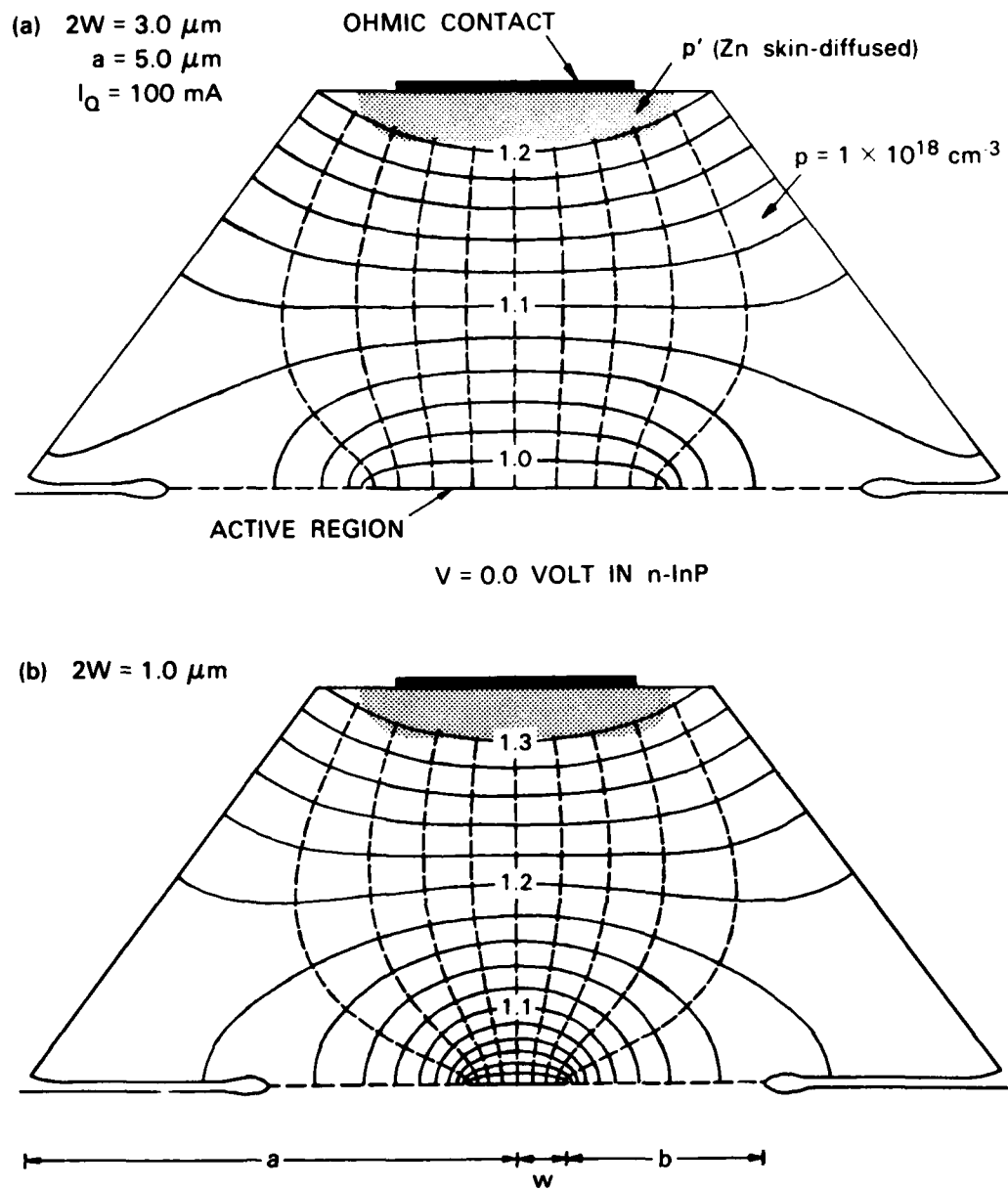


Figure 1-3. Calculated voltage distribution for two laser mesas with different active region widths. Equipotentials are separated by equal voltage increments; numbers are in volts. Dashed curves are the streamlines.

where A_H is the effective homojunction area, D_n and L_n are electron diffusivity and effective diffusion length, respectively, n_i is the intrinsic carrier concentration, k is the Boltzmann constant, and $V_H = V(W + b, 0)$ with b being the transported region width. The effective homojunction area is defined as $A_H = 2L\Delta b$, with the effective width $\Delta b = \int_W^{W+b} \exp [qV(u, 0)/kT] du / \exp (qV_H/kT)$, which can be estimated to be approximately the distance in which $V(u, 0)$ reduces by kT/q or (as done here) evaluated precisely by numerical integration. In the following calculations $D_n = 78 \text{ cm}^2/\text{s}$ and $n_i^2 = 1.6 \times 10^{14} \text{ cm}^{-6}$ were used, as computed from published carrier-transport and band-structure parameters,⁴ and a constant $L_n = 7 \text{ }\mu\text{m}$ was assumed.

TABLE 1-1

Calculated I_H and Related Parameters as a Function of I_Q
for $p = 4 \times 10^{17} \text{ cm}^{-3}$, $a = 5.0 \text{ }\mu\text{m}$, $W = 1.5 \text{ }\mu\text{m}$, and $b = 2.0 \text{ }\mu\text{m}$

I_Q (mA)	V_H (V)	Δb (μm)	$n_p(0)^*$ (cm^{-3})	I_H (mA)	I_1 (mA)	I_2 (mA)
20	1.03	1.37	7.15×10^{13}	0.0732	53.9	12.9
40	1.08	1.08	4.56×10^{14}	0.368	52.3	12.2
60	1.13	0.87	3.03×10^{15}	1.96	52.0	11.9
80	1.17	0.75	1.93×10^{16}	10.9	52.3	11.6
100	1.22	0.65	1.28×10^{17}	62.0	52.7	11.5
* $n_p(0) = \frac{n_i^2}{p} \exp \left[\frac{qV_H}{kT} \right]$						

Table 1-1 shows calculated I_H and related physical parameters as a function of I_Q on a given device. Note that I_H is initially very small but increases exponentially. When $I_H \approx I_Q$, voltage along the InP homojunctions calculated for I_Q alone may remain a fair approximation, because the additional electric field for the hole-drift-current component of I_H is small up to approximately one electron-diffusion length away from the homojunctions and is therefore not expected to significantly affect the homojunction voltage. The effect of the calculated homojunction current on an otherwise linear L-I characteristic is demonstrated in Figure 1-4, which was obtained by adding I_H to I_Q for each power output. To facilitate comparison with experiment, Equations (1-3) and (1-4) can be combined and rearranged into

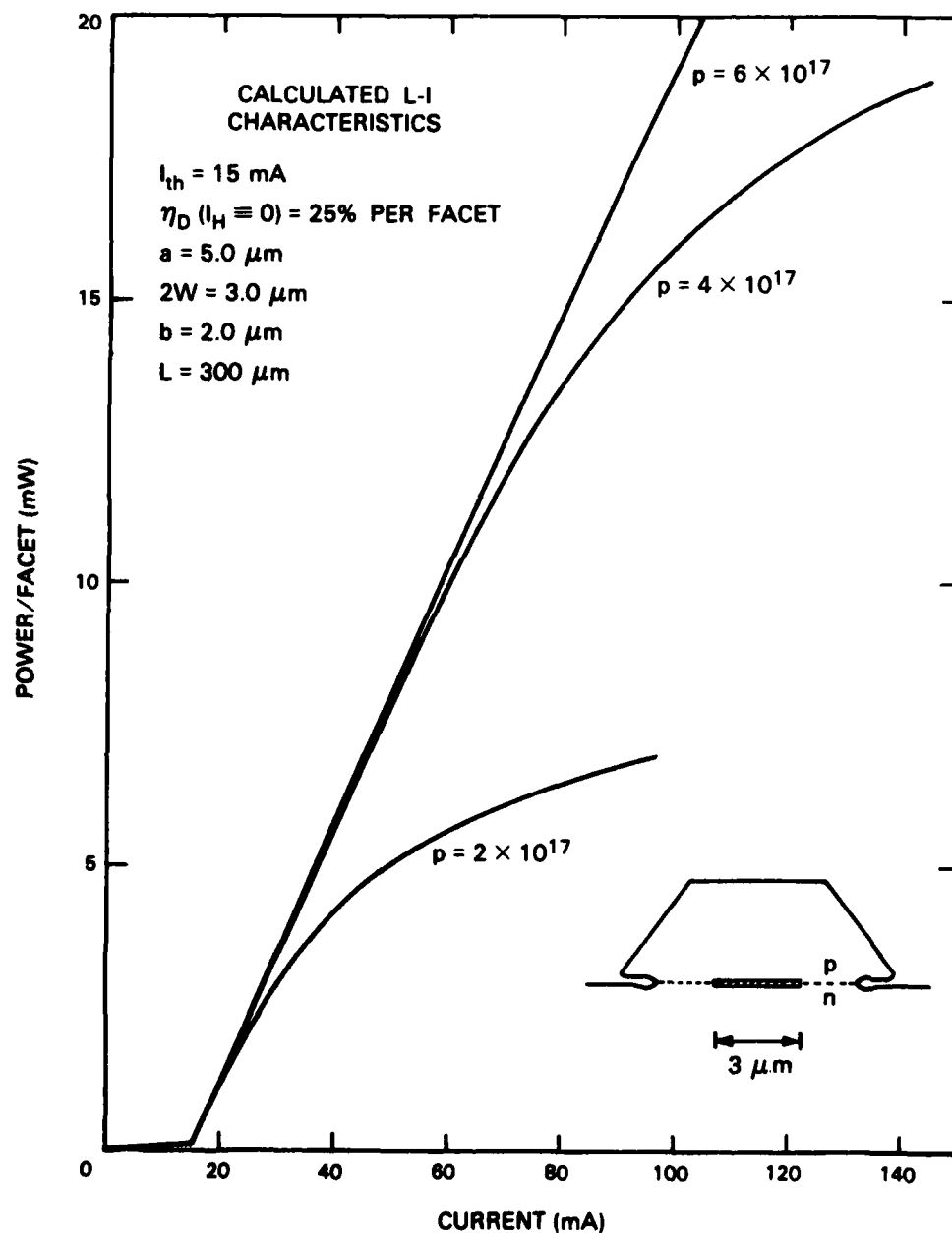


Figure 1-4. Sublinear L-I characteristics resulting from adding the homojunction current to a linear one. Calculation of the homojunction current was carried out for the device geometry shown in the insert and for three different p-doping concentrations. Note that the numerical values of the curve of $p = 4 \times 10^{17} \text{ cm}^{-3}$ are listed in Table 1-1.

$$I_H = 1 \text{ mA} \cdot \exp [(I_Q - I_1)/I_2] \quad (1-5)$$

where I_1 and I_2 are parameters characteristic of the device and are nearly independent of I_Q (cf. Table 1-1). Note that I_1 is essentially the value of I_Q at which I_H becomes significant ($I_H = 1 \text{ mA}$). The functional form of Equation (1-5) is in good agreement with experiment.

Figure 1-5 shows calculated I_1 as a function of p for $a = 5.0 \text{ } \mu\text{m}$, $b = 2.0 \text{ } \mu\text{m}$ and three values of W . The experimental values of I_1 for $p \leq 3 \times 10^{17} \text{ cm}^{-3}$ were 15 to 26 mA, in general agreement with Figure 1-5. A more accurate comparison, however, is not available at present because of the uncertainties in both theory and experiment.

In conclusion, the conformal mapping technique allows for rather accurate calculation of the voltage distribution in the laser mesa. The present theory is valuable for designing lasers for operation without current leakage through the forward-biased homojunctions.

Z.L. Liao
J.N. Walpole
D.Z. Tsang

1.2 LINEAR LIGHT-CURRENT CHARACTERISTICS IN MASS-TRANSPORTED GaInAsP/InP BURIED-HETEROSTRUCTURE LASERS

Linear light-output-current (L-I) characteristics and high-power operation are important for heterostructure lasers. In this work mass-transported GaInAsP/InP buried-heterostructure (BH) lasers with low threshold currents and linear light output to greater than 13 mW/facet have been obtained. This is achieved by using sufficient p-doping in the cap layer of the starting double heterostructure wafer, a technique simpler than the previously reported one⁵ in which Zn-diffusion was employed.

Five wafers were grown with the p-doping ranging from 2.5×10^{17} to $2.3 \times 10^{18} \text{ cm}^{-3}$. (The corresponding Zn concentration in the liquid-phase epitaxial growth was calibrated by using Hall-effect measurements on 8- μm -thick InP layers grown on semi-insulating substrates.) A trend of improved L-I linearity with increasing doping was observed, as shown in Figure 1-6. Essentially linear characteristics up to the maximum operation current of 75 mA were obtained for wafers with $p \geq 9.1 \times 10^{17} \text{ cm}^{-3}$. Such linearity was never achieved for devices fabricated from six lightly doped wafers ($p \leq 3 \times 10^{17} \text{ cm}^{-3}$), including the earlier ones.

However, a trend of increasing threshold current was also observed. For example, devices fabricated from wafers with $p = 9.1 \times 10^{17}$ and $2.3 \times 10^{18} \text{ cm}^{-3}$ showed overall threshold current increases of ≈ 50 and 200 percent, respectively, as compared with those of $p = 2.5 \times 10^{17} \text{ cm}^{-3}$. (The active region dimensions were presumably quite similar in these wafers.) It should be noted that increase in threshold current with the p-doping has previously been reported for broad area lasers.^{6,7} In this work, an attempt to preserve the low threshold current was made by growing Wafer 635 with a thin ($\approx 0.4 \text{ } \mu\text{m}$) lightly doped

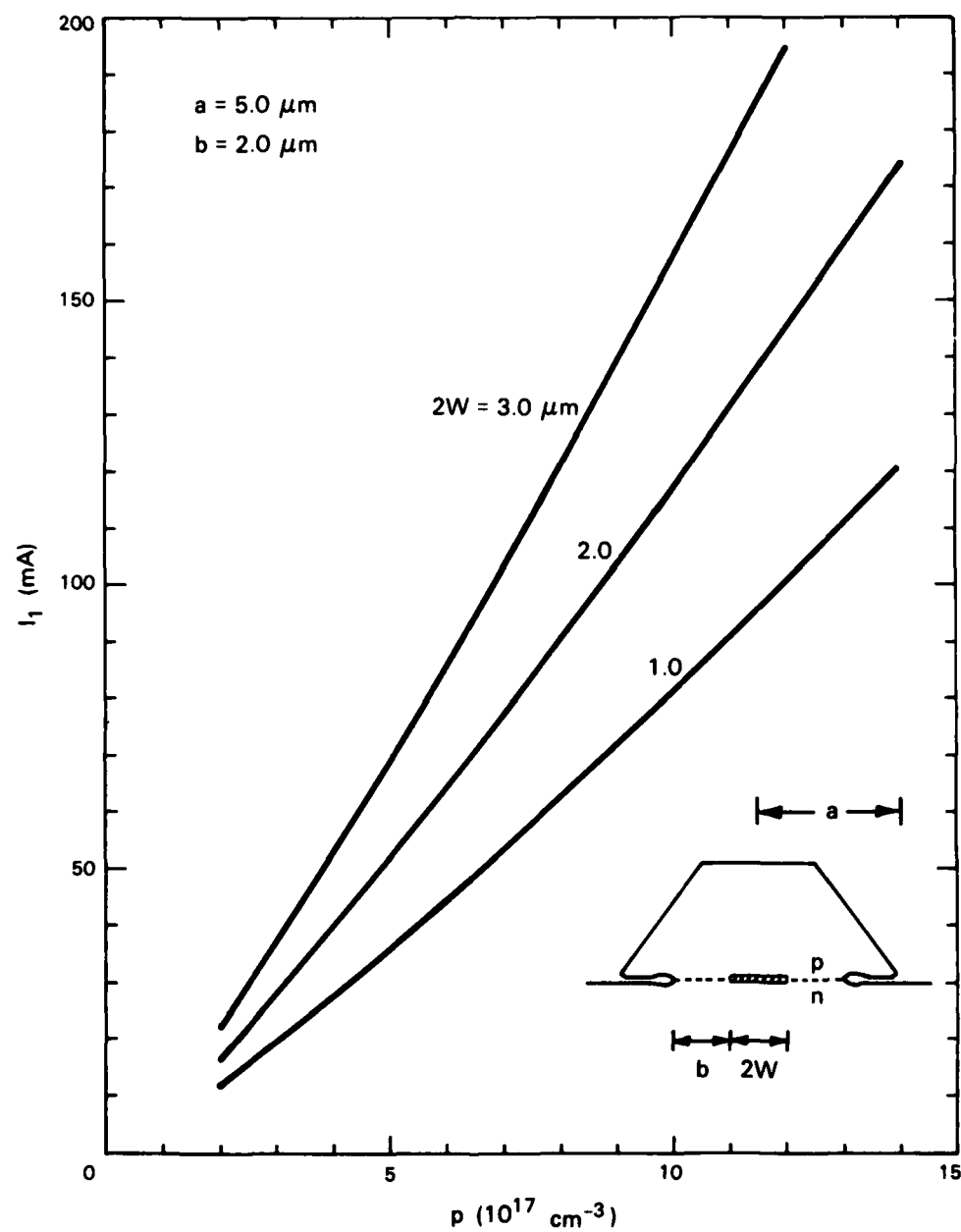


Figure 1-5. Calculated I_1 as a function of the cap p-doping.

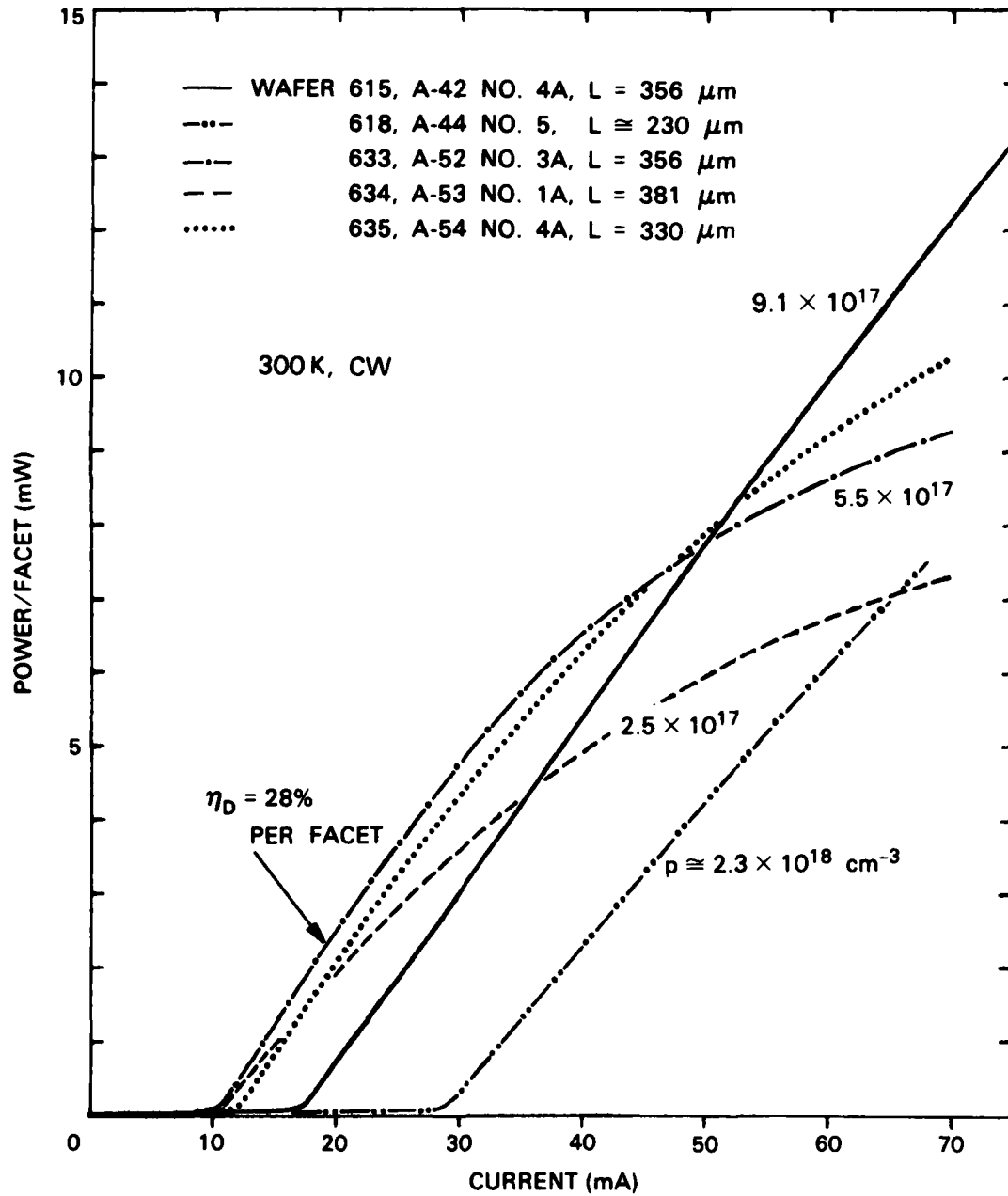


Figure 1-6. L-I characteristics of five mass-transported BH lasers with different cap-layer doping concentrations. These devices were mounted p-side down.

InP layer between the active layer and the heavily doped cap ($p \cong 7.9 \times 10^{17} \text{ cm}^{-3}$). This wafer resulted in threshold currents 11 to 16 mA (similar to those of lightly doped ones) as well as an improved L-I linearity (see the dotted curve in Figure 1-6).

Figure 1-7 shows far-field patterns in the junction plane. These far-field patterns are smooth compared with those of the more conventional BH lasers,⁸ and single lateral mode operation was maintained up to the maximum operation current of 60 mA, nearly three times the threshold current. Other devices showed a full angular width at half maximum intensity as narrow as 23° , corresponding to an active region of estimated $3\text{-}\mu\text{m}$ width and $0.15\text{-}\mu\text{m}$ thickness.

The improvement of L-I linearity with p-doping is consistent with the hypothesis of the forward-biased InP homojunctions described in the previous report.⁵ (For a more rigorous treatment of the homojunction problem, see Section 1.1.) However, it does not rule out other possible causes such as the electron leakage over the heterobarrier.⁹⁻¹¹ This latter mechanism has been invoked to explain the threshold-temperature dependence in GaInAsP lasers, but its possible consequences on the L-I characteristics were not discussed.⁹⁻¹¹

Z.L. Liao
J.N. Walpole
D.Z. Tsang

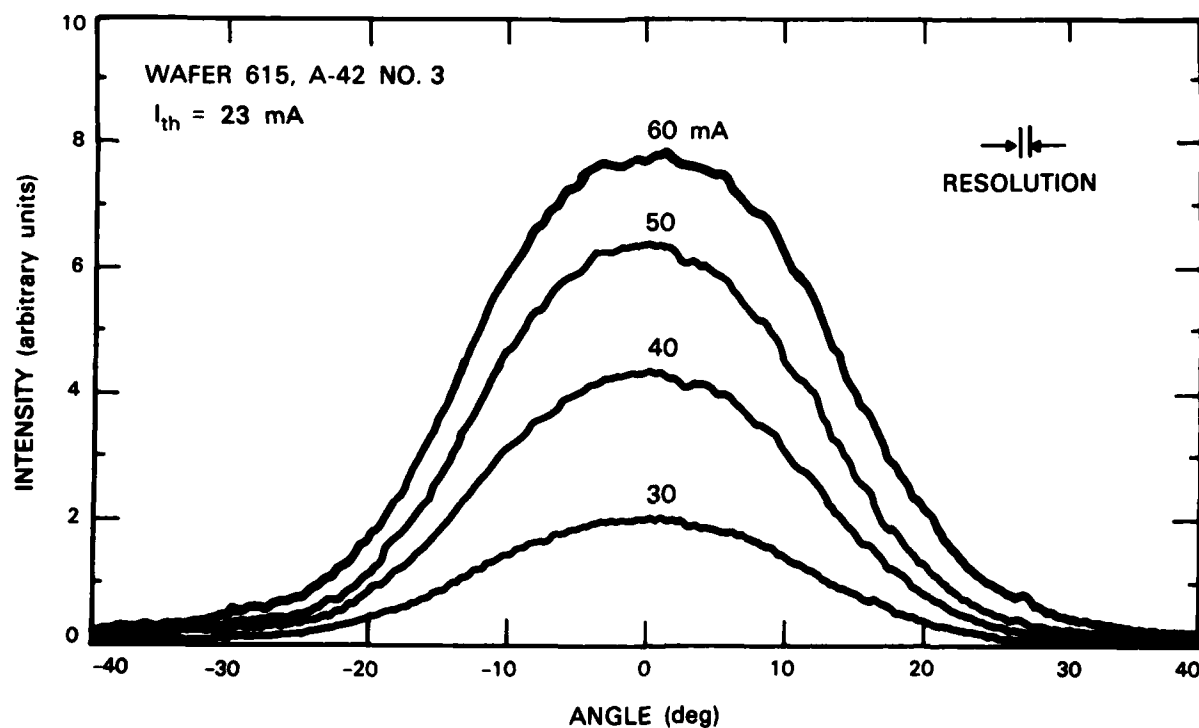


Figure 1-7. Far-field patterns in the junction plane of a mass-transported BH laser.

1.3 FOUR-ELEMENT 10.6- μm PHOTOMIXER ARRAYS OPERATING AT 195 K

Linear arrays of p-type HgCdTe photoconductors have been developed for elevated-temperature heterodyne operation at 10.6 μm . This array work is an extension of the single-element elevated-temperature photomixer work previously reported.^{12,13} A photograph of an array of detectors is shown in Figure 1-8. The individual detectors are approximately $50 \times 50 \times 2 \mu\text{m}$ thick and spaced on 100- μm centers. At 195 K, the detector cutoff wavelength was about 13 μm .

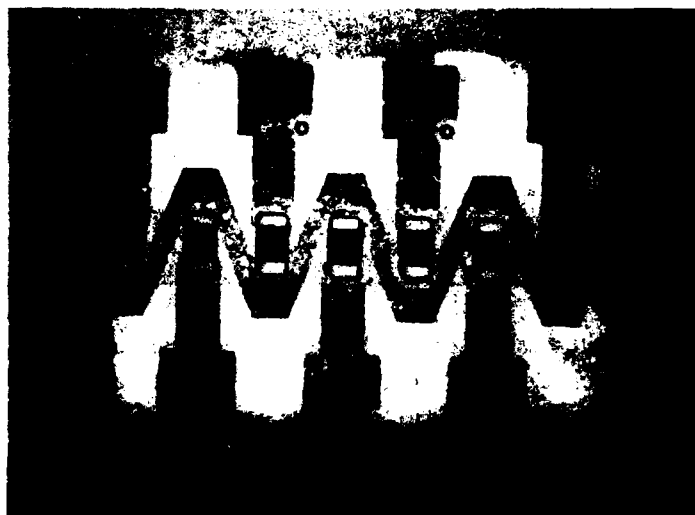


Figure 1-8. Photograph of a linear array of p-type HgCdTe photoconductors designed for 10.6- μm heterodyne operation at 195 K.

Heterodyne performance characteristics of a 4-element array of HgCdTe photoconductors are listed in Table 1-2. All four devices in this array were found to have an NEP = 3.5×10^{-19} W/Hz at 40 MHz when illuminated with a 3-mW CO₂ laser local oscillator beam (LO). The measurement uncertainty was ± 10 percent, and is therefore the upper limit of the nonuniformity. The bandwidth, as determined by G-R noise measurements, increased with LO power, from 165 MHz at zero power to 420 MHz at a power level of 22 mW. This increase is due to the high photoelectron concentration produced by the LO, which increases the probability of Auger recombination. Maximum heterodyne sensitivity was achieved with an LO power of 3 mW, and here the detector bandwidth was about 250 MHz. In this temperature region there is a strong trade-off between sensitivity and bandwidth.¹³ An average array NEP of 1×10^{-19} W/Hz should be achieved by lowering the hole concentration so as to reduce the bandwidth to about 100 MHz.

Cross-talk was measured by illuminating one detector and measuring the RF signal from an adjacent device. At 40 MHz, this cross-talk was found to be -35 dB, and is believed to

TABLE 1-2 4-Element Photomixer Array Performance at 195 K	
Average NEP at 10.6 μm ($P_{\text{LO}} = 3 \text{ mW}$)	$3.5 \times 10^{19} \text{ W/Hz}$
Nonuniformity	$< \pm 10\%$
Bandwidth	250 MHz
Cross-Talk	-35 dB
Total Dissipation	36 mW

be primarily due to the finite resistance in the common meander-line ground (see Figure 1-8). At maximum sensitivity, each detector required a bias power of 6 mW and an LO power of 3 mW, giving a total dissipation of 36 mW for the 4-element array. This power dissipation level is compatible with the cooling capability of standard 4-stage thermoelectric coolers.

D.L. Spears

REFERENCES

1. W.R. Smythe, *Static and Dynamic Electricity*, 3rd Edition (McGraw-Hill, New York, 1968), p. 90.
2. F.B. Hildebrand, *Advanced Calculus for Applications* (Prentice-Hall, New York, 1962), p. 574.
3. N.K. Dutta, J. Appl. Phys. **51**, 6095 (1980); J. Appl. Phys. **52**, 55 (1981).
4. T.P. Pearsall, Ed., *GaInAsP Alloy Semiconductors* (Wiley, New York, 1982), p. 308.
5. Solid State Research Report, Lincoln Laboratory, M.I.T. (1983:1), pp. 1-5, DTIC AD-A128894/3; and Z.L. Liau, J.N. Walpole, and D.Z. Tsang, *Technical Digest, IOOC '83* (IECE of Japan, Tokyo, 1983), p. 152.
6. Y. Itaya, Y. Suematsu, S. Katayama, K. Kishino, and S. Arai, Jpn. J. Appl. Phys. **18**, 1795 (1979).
7. W. Ng and Y.Z. Liu, Electron. Lett. **16**, 693 (1980).
8. I. Mito, M. Kitamura, Ke. Kobayashi, S. Murata, M. Seki, Y. Odagiri, H. Nishimoto, M. Yamaguchi, and Ko. Kobayashi, IEEE J. Lightwave Technol. **LT-1**, 195 (1983).
9. P.J. Anthony and N.E. Schumaker, J. Appl. Phys. **51**, 5038 (1980).
10. C.B. Su, J. Schlafer, J. Manning, and R. Olshansky, Electron. Lett. **18**, 1108 (1982).
11. T.R. Chen, B. Chang, L.C. Chiu, K.L. Yu, S. Margalit, and A. Yariv, Appl. Phys. Lett. **43**, 217 (1983).
12. D.L. Spears, Technical Report TR-81-1129, AFWAL AADO-3, Wright-Patterson Aeronautical Laboratories (March 1981); and Solid State Research Report, Lincoln Laboratory, M.I.T. (1980:3), DTIC AD-A094075/9.
13. D.L. Spears, Proc. IRIS Specialty Group on Infrared Detectors, 27-30 August 1982, San Diego, California; and Solid State Research Report, Lincoln Laboratory, M.I.T. (1982:4), DTIC AD-A128982/6.

2. QUANTUM ELECTRONICS

2.1 ANALYTICAL COMPARISON OF OPTIMIZED HETERODYNE AND DIRECT-DETECTION LIDAR FOR ATMOSPHERIC REMOTE SENSING

Recently an experimental study¹ of the relative merits of heterodyne and direct-detection CO₂ DIAL for path-averaged remote sensing was carried out using LIDAR backscattered returns from topographic targets. In these studies, the average signal-to-noise ratios and statistical and temporal characteristics of the LIDAR returns were measured simultaneously for both detection techniques. The experimental results were found to be in good agreement with a simple analysis which predicted the relative sensitivity of each detection technique for path-averaged measurements. The detection systems used in these experiments were not optimized for either technique.

We now have made a similar, but generalized, analytical comparison of heterodyne and direct detection for an optimized pulsed CO₂ DIAL system which is constrained by several factors including weight, system complexity, and input energy considerations. In addition, the comparison has been directed toward range-resolved remote sensing using LIDAR signals backscattered from atmospheric aerosols.

Previous work indicated that the accuracy of a DIAL measurement is limited at close-in ranges (where LIDAR signal returns are strong) by the level of fluctuations of the LIDAR return signals, and at far ranges by the noise equivalent power (NEP) of the detector.¹ The approximate equations which describe these limitations are given for close-in ranges by

$$N_{\min} \approx \sigma_n / (2\sigma_a \Delta R) \quad , \quad (2-1)$$

and for far ranges by

$$N_{\min} \approx \frac{1}{2\sigma_a \Delta R} \frac{1}{(P_r / \text{NEP})} \quad (2-2)$$

where N_{\min} is the minimum concentration of the species that can be detected, σ_n is the signal-averaged standard deviation of the LIDAR signal fluctuations, σ_a is the absorption cross section of the absorbing atmospheric species, ΔR is the range resolution, and P_r is the signal power of the pulsed LIDAR return.

Equations (2-1) and (2-2) define the approximate limits of measurement accuracy of a DIAL system. Equation (2-1) sets the limits due to fluctuations in the LIDAR returns caused by target, speckle, or atmospheric effects, even though the average signal-to-noise ratio (SNR) or carrier-to-noise ratio (CNR) is high. Equation (2-2) determines the additional constraints on the accuracy when CNR becomes less than or equal to 1.

Equations (2-1) and (2-2) represent limits of a more general theory,² and are essentially correct in the region of validity of the analysis, i.e., at close-in and far ranges, respectively.

For the numerical prediction of the system performance of both heterodyne and direct-detection CO₂ LIDAR systems it is convenient to use the mathematical notation of Shapiro² to describe the combined influence of signal fluctuations and low CNR. In this case, one calculates the CNR value and the saturated value (predicted fluctuation-dominated value), SNR_{SAT}, to deduce the resultant SNR value.

The value of the predicted measurement accuracy, σ_n , is then determined from

$$\sigma_n = \frac{1}{F} \frac{1}{\sqrt{\text{SNR}}} \quad (2-3)$$

where F is the signal-averaging improvement factor, which would be equal to $N^{1/2}$ for statistically independent samples; N is the number of pulses integrated.

In order to make a realistic comparison of different LIDAR systems, one must consider the system requirements as well as any other constraining factors. Toward this end, we consider system parameters appropriate for a compact, 10- μm CO₂ DIAL system for short-range (<5 km), range-resolved measurement for species concentration in the atmosphere. In addition, constraining factors are given which include realistic limitations for primary input electrical power, volume, weight, signal-processing time, and system complexity.

Table 2-1 gives parameter values of two possible DIAL systems using heterodyne detection and direct detection. The reasons for selecting the parameter values shown and the differences between the heterodyne and direct-detection cases are presented in Reference 3.

Most significantly, it is demonstrated in Reference 3 that the direct-detection system can be substantially improved by the use of a cold IR filter so that the detector is not background-limited, the use of a matched, cooled, state-of-the-art amplifier, and hybrid integration of the amplifier with a photovoltaic (photodiode) HgCdTe detector.⁴ Specially passivated HgCdTe detectors have been developed, but have yet to be integrated with an optimized amplifier.⁵ The construction of such a detector/amplifier combination would entail a moderate development program but should be technically feasible.

An analysis was made of the expected measurement accuracy as a function of range for the two DIAL systems shown in Table 2-1. The calculations were made with both systems operating at a PRF of either 100 or 10,000 Hz.

Figure 2-1 shows the calculated σ_n values for the two systems assuming an integration time of 1 s and $F = N^{1/2}$. Two important conclusions may be obtained from Figure 2-1. First, similar performance is predicted for the 100-Hz PRF direct-detection system and the 10,000-Hz PRF heterodyne-detection system. Second, these respective PRF values offer the best compromise between close-in measurement accuracy and long-range detection.

In conclusion, the analysis has shown some of the design trade-offs between heterodyne and direct-detection DIAL systems, with specific application to range-resolved remote sensing of atmospheric species. The results indicate that acceptable performance may be obtainable

TABLE 2-1		
List of Parameter Values for the Two Baseline DIAL Systems*		
Parameters	Heterodyne	Direct
Average Laser Power (W)	3	10
Laser Modes	1	5
Pulse Length (ns)	350	350
Bandwidth (MHz)	3	3
Transmitted Beam Diameter (m)	0.15	0.06
Receiver (Telescope) Diameter (m)	0.15	0.30
NEP (Optimized) (W)	0.6×10^{-13}	0.9×10^{-11}
PRF (Hz)	100/10,000	100/10,000
Range Resolution	50 m	
Atmospheric Backscatter	$1 \times 10^{-7} \text{m}^{-1} \text{sr}^{-1}$	
Optical Efficiency	0.1	
Atmospheric Attenuation	0.12 km^{-1} (0.5 dB/km)	
Signal Averaging Time	1 s	
*Each system has a PRF of 100 or 10,000 Hz, which directly affects the peak transmitted power.		

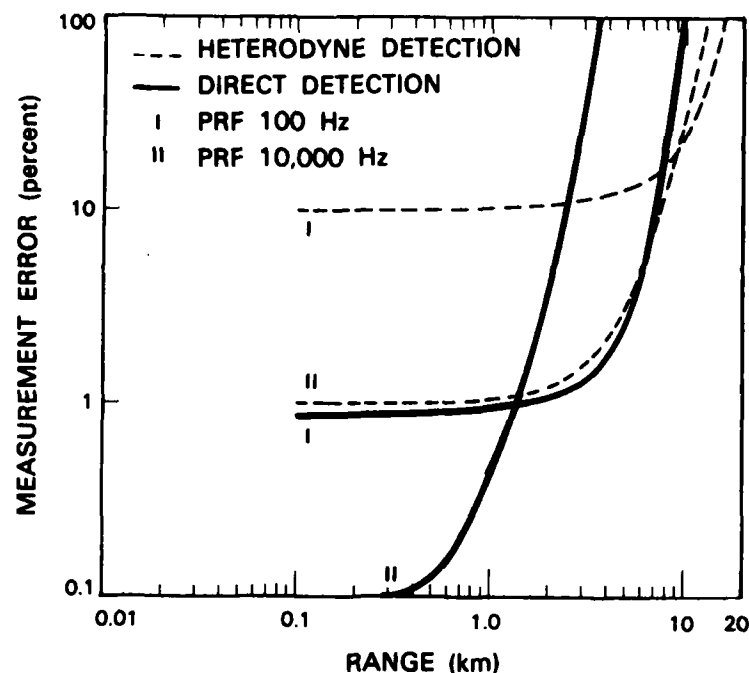


Figure 2-1. Predicted percentage measurement error, σ_n , as a function of range for the baseline LIDAR systems.

with a direct-detection system if a significant improvement in detector/amplifier technology is accomplished. Such improvement is technically feasible. In addition, the results have shown the importance of a reasonable choice of the particular constraints applicable to each system. This contrasts with a rigid comparison of similar systems, which does not allow for differences in the PRF, average laser power, laser mode structure, or receiver/detector characteristics.

Finally, it should be emphasized that the values of σ_n shown in Figure 2-1 are theoretical predictions and have not been experimentally verified. Future experimental work will be required in order to establish the validity of some of these predictions and the feasibility of the hardware development.

D.K. Killinger
N. Menyuk

2.2 SURFACE-PHOTOACOUSTIC-WAVE SPECTROSCOPY

We have reported previously^{6,7} on the detection of surface acoustic waves (SAW) generated by relaxation of energy optically absorbed in thin surface films. The reported detection sensitivity was an absorbance of 5×10^{-5} of the laser energy with a maximum laser energy density of 0.1 J/cm^2 , limited by the desorption of the molecular film. We now report on improvements of several orders of magnitude in the minimum detectable absorption coefficient. Two techniques have been used to achieve this improvement: (a) use of a 50-MHz

center frequency edge-bonded transducer (EBT), and (b) use of multiple image spots to increase the acoustic energy without exceeding the damage-limited laser fluence.

In order to insure that the SAW signals from different spots on the sample reach the transducer in the same phase, the laser beam is focused to a line image parallel to the edge of the substrate with the transducer. The center frequency of the generated SAW signal is set by the laser spot size, with $\omega = v/2w$, where v is the acoustic velocity (3×10^5 cm/s) and $2w$ is the beam waist (~ 30 μ m). For optimum sensitivity, this frequency should match the transducer center frequency. An additional constraint for efficient SAW generation is that the laser pulse duration should be short compared to the acoustic transit time across the laser spot. Both of these criteria are more easily satisfied at lower frequencies. Our initial measurements were carried out using a 130-MHz center-frequency transducer; shifting to a 50-MHz center-frequency EBT without modifying the optical arrangement yielded an improvement in the minimum detectable absorbance of approximately one order of magnitude to 5×10^{-6} of the laser energy. Figure 2-2 shows the output SAW signal vs input

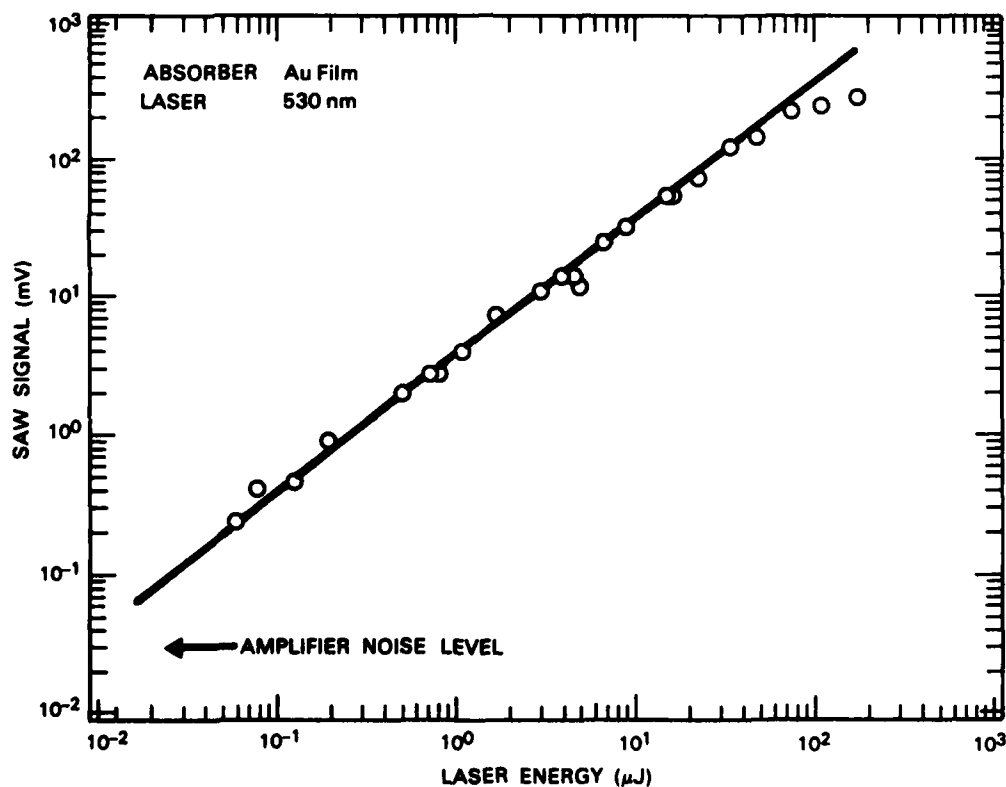
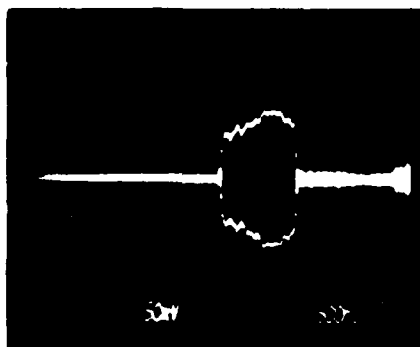
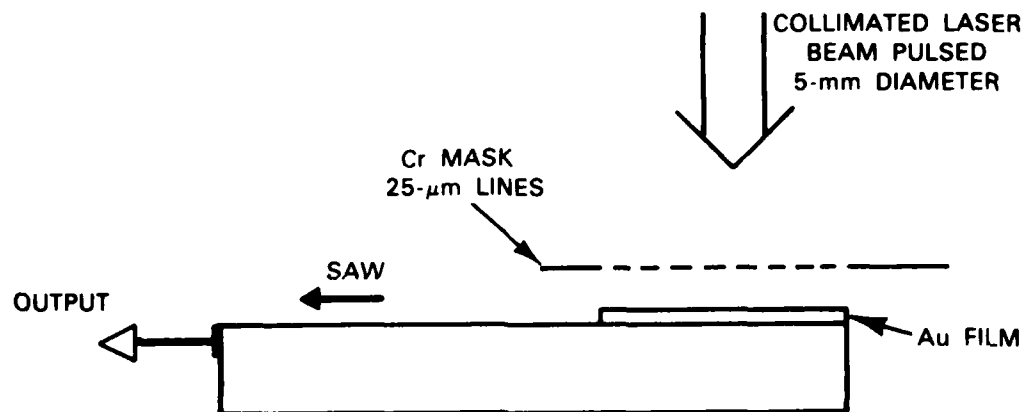
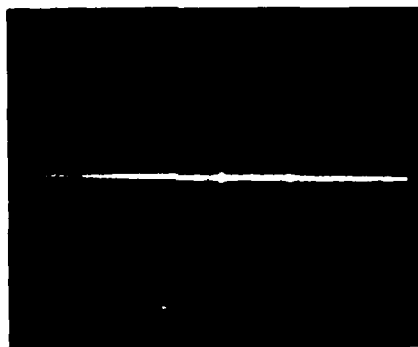


Figure 2-2. Linearity of SAW signal vs laser energy for 530-nm irradiation of a 200-nm-thick Au film. The solid line has unity slope.



OUTPUT WITH
MASK



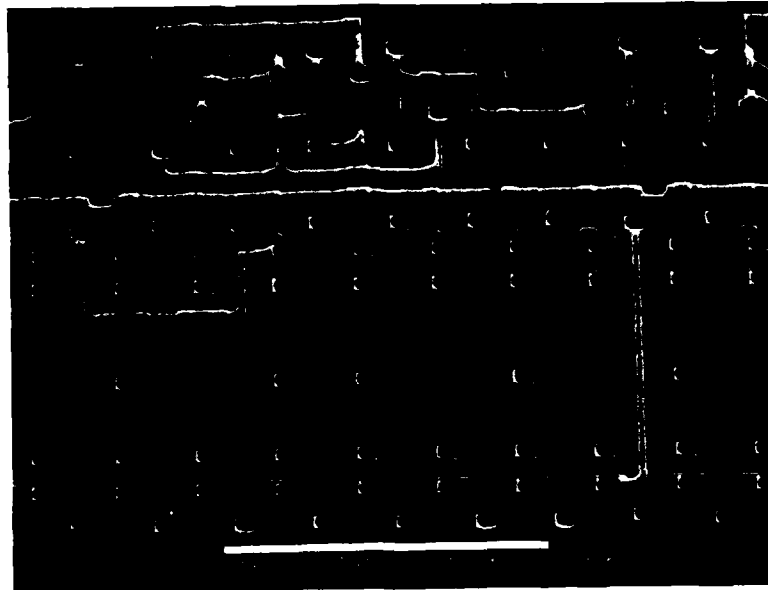
OUTPUT WITHOUT
MASK

Figure 2-3. Output of EBT with multiple spot illumination. (Top) through 3- \times 4-mm shaping aperture and 50- μ m-period Cr mask; (bottom) Cr mask removed.

laser energy for a 50-MHz center-frequency EBT on a ST-quartz substrate with a 200-nm-thick gold film absorber. The SAW signal is in peak-to-peak volts at the EBT. Plotted are the measured points and a straight line of unity slope. The output voltage is proportional to the input energy over more than three orders of magnitude in voltage or more than 60 dB in power. The saturation observed at high SAW signal levels is most likely due to a nonlinear absorption process since the SAW level at the compression point is too low to lead to acoustic nonlinearities in either the substrate or the EBT.

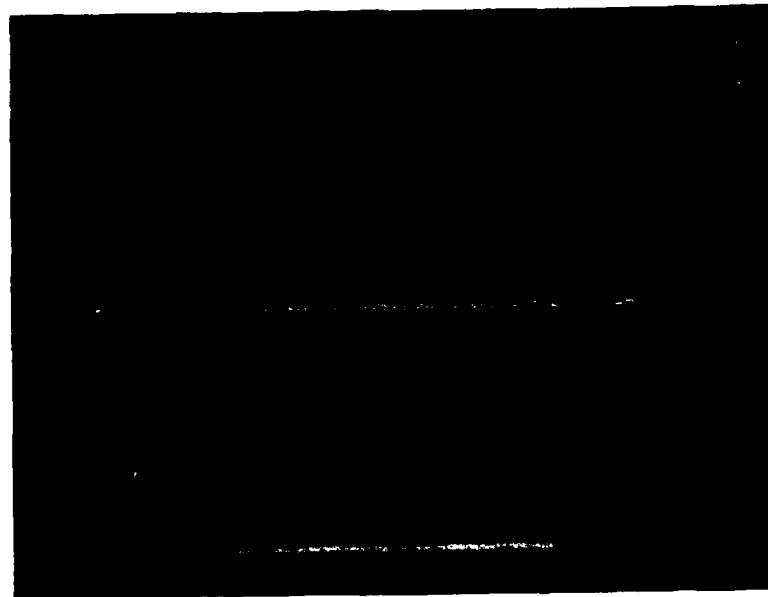
All of these results were obtained using a single line image. Substantially more laser energy is available, but is not usable in this configuration since either the absorption process becomes nonlinear or the film is damaged at higher laser fluences. To increase the detection sensitivity we have employed the multiple line image technique illustrated in Figure 2-3. A 5-mm-dia. collimated laser beam was used to illuminate the absorber on the substrate. The beam passed through a mask with a shaping aperture of 3×4 mm and a grating of 25- μ m lines and 25- μ m spaces; the illumination pattern on the surface is a series of bright and dark lines. This pattern acts like an interdigital transducer to produce a pulse of SAW energy over the entire illuminated area. Figure 2-3 shows the SAW pulse generated by this technique using the same Au film and 50-MHz EBT transducer. The time duration of the output simply corresponds to the SAW transit time across the spatial extent of the laser spot. With the grating removed, but still with the shaping aperture, very little high-frequency SAW signal was generated. The dominant residual signals originate at the edges of the 3-mm aperture and at imperfections in the Au film. Straightforward signal-to-noise calculations show that this multiple spot technique improves the sensitivity by the square root of the number of cycles in the resulting SAW signal. This is a factor of 25 for the present experiment. An additional factor of 10 improvement in the SAW signal over that obtained in the single spot experiments was observed, using a fixed laser fluence. This is probably due to a better coupling of the present sharply defined 25- μ m lines than of the single 30- μ m Gaussian spot to the 50-MHz SAW. These improvements bring the minimum detectable absorbance to 2×10^{-8} of the laser energy. An additional advantage of the multiple spot technique is the discrimination against background absorption of the substrate. If the thin film absorber is patterned, either lithographically or by laser processing, any unpatterned absorption in the substrate is automatically discriminated against in the SAW generation process. This will allow investigation of many interesting systems such as adsorbates on metal films in which the substrate absorption would otherwise mask the adsorbate signals. Further development of these techniques and the use of signal averaging electronics will improve the detection sensitivity even further. We are presently pursuing the application of SAW detection to the measurement of absorption in interesting semiconductor systems such as quantum-well structures and thin-film nucleation problems.

S.R.J. Brueck
T.F. Deutsch
D.E. Oates



BEFORE

(a)



AFTER

(b)

Figure 2-4. SEMs of a portion of a ring oscillator (a) before and (b) after laser-microchemical restructuring. One short vertical Al link has been removed, and one long horizontal poly-Si link has been added.

133483-R-01

2.3 LASER MICROCHEMICAL TECHNIQUES FOR REVERSIBLE RESTRUCTURING OF GATE-ARRAY PROTOTYPE CIRCUITS

During the last several years there has been growing interest in special methods for fabricating or altering integrated-circuit prototypes. For example, it has been demonstrated that e-beam and laser-beam direct wafer writing which avoid lengthy photomask tooling can be valuable both in the early stages of circuit design and testing as well as in fault avoidance during the final stage of the fabrication of complex circuits. Below we describe initial applications of laser microchemical modification techniques to this class of problems.

Laser-microchemical techniques for direct deposition and etching make use of tightly focused visible and UV beams to drive localized surface chemical reactions.⁸ Recently the first applications of these processes to device fabrication were reported.⁹ Here, in this initial demonstration of *circuit* restructuring, test circuits were reconfigured by severing discretionary Al interconnects using laser-controlled chemical vapor deposition. The starting circuit for this work was a 500-gate CMOS gate array manufactured using 5- μm design rules. The discretionary metal interconnect pattern, fabricated by conventional photolithography and dry etching, personalized the array into simple test structures such as ring oscillators, comparators, and logic gates.

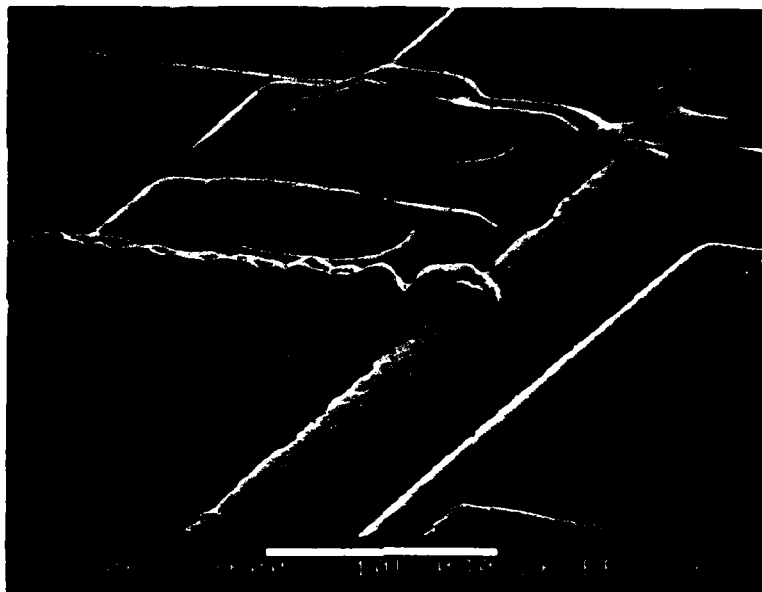
The laser-writing instrument itself has been described in detail elsewhere.⁸ Briefly, it consists of a high-power microscope through which a laser beam is directed onto the circuit. Patterns are drawn by moving the workpiece with computer-controlled translation stages driven by DC motors. For the modest resolution needed in the current experiment, a 488-nm TEM₀₀ Ar-ion laser beam was focused to a nominal 3- μm -dia. spot using f/8 refractive optics. The laser deposition¹⁰ and etching¹¹ processes also have been described previously. Briefly, the etching process for Al involves localized, modest (<200°C) laser heating of a surface bathed in a capillary liquid etchant layer trapped between the Si wafer and a thin cover glass. The deposition process occurs by localized laser heating of a surface in a 200-Torr ambient of silane vapor. This induces the chemical vapor deposition of heavily B-doped poly-Si, suitable for forming ohmic contacts to Al. Laser scan rates for deposition of 1.5- μm -thick conductors are $\sim 75 \mu\text{m/s}$. In order to avoid damage to active devices, the poly-Si interconnects were routed away from channel regions. Submicrometer linewidths have been demonstrated using similar microreactions and tighter focusing.

Figure 2-4 shows scanning electron micrographs (SEMs) of a section of a ring oscillator circuit before and after restructuring. The Al metallization at the left of Figure 2-5(a) connects the eighth to the ninth gate in the ring oscillator. In Figure 2-5(b), this conductor is shown severed by laser etching.

Also shown in Figure 2-4(b) is a laser-deposited poly-Si conductor which connects the eighth to the thirteenth gate in the oscillator, thereby decreasing the number of stages from 23 to 19. Magnified details of the morphology of the poly-Si are shown in Figure 2-5. The step coverage, shown in Figure 2-5(a), is very good, and is characteristic of laser deposition



(a)



(b)

Figure 2-5. SEMs of doped poly-Si lines deposited using laser microchemistry onto gate-array chip, showing (a) step coverage and (b) formation of contact with Al. The bars in (a) and (b) indicate 1- and 10- μ m lengths, respectively.

133461-R

processes even over high steps. A contact to an Al line is shown in Figure 2-5(b). Although the poly-Si deposition temperature exceeds the Al-metallization melting point, the lateral laser-induced temperature profile is well localized and no apparent damage to the existing Al conductors is observed. Contact formation is thought to occur through an alloying reaction.

In a separate experiment, Al/poly-Si contact resistances and poly-Si sheet resistances were measured by laser-depositing poly-Si to interconnect Al pads separated by various distances. From the intercept of the resulting plot of resistance vs poly-Si length, contact resistances were found to be $<10\ \Omega$ for a typical $3\text{-}\mu\text{m} \times 3\text{-}\mu\text{m}$ contact area; the film resistivity is $\approx 3 \times 10^3\ \Omega\text{-cm}$, comparable to that of conventionally formed B-doped poly-Si. No furnace annealing or other treatment was used after any of the laser operations.

Electrical characteristics of a representative ring oscillator before and after a 23- to 19-stage restructuring are shown in Figure 2-6. Similar oscillation waveforms were observed both before and after [Figure 2-6(b)] the laser modification. Typical delays are $\sim 4\text{ ns/stage}$. The before and after oscillation period vs supply voltage plots [Figure 2-6(a)] are identical except for a proportionate reduction by the ratio 23/19. Similar proportionate reductions were found for 23- to 15-stage restructurings. In a separate test a $30\text{-}\mu\text{m}$ -long Al conductor was severed and then replaced by laser-deposited poly-Si; the oscillation period vs supply voltage plots were the same to within 3 percent. No significant degradation of circuit performance due to the larger resistivity of poly-Si compared with Al, or to the poly-Si/Al contacts, were observed. This was as expected, since for these restructurings, the extra RC time due to the typically 10 squares of poly-Si over $1\text{-}\mu\text{m}$ -thick oxide is less than $\sim 12\text{ ps}$. This number increases with the interconnect length, however, and for more than 100 squares of the poly-Si may begin to be significant ($>1\text{ ns}$). In such cases, however, poly-Si deposition may still find application in debugging complex architectures, while clocking at lower frequencies. Further experiments will explore the uses of these techniques for wafer-scale restructurable VLSI and for isolation and testing of circuit substructures within VLSI prototypes.

D.J. Ehrlich	J.H.C. Sedlacek
J.Y. Tsao	D.J. Sullivan
D.J. Silversmith	R.W. Mountain

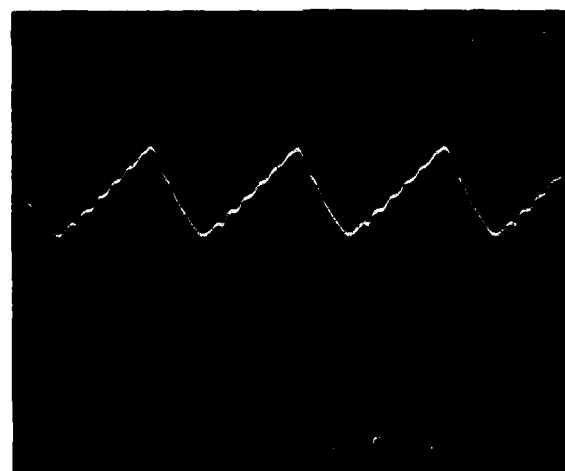
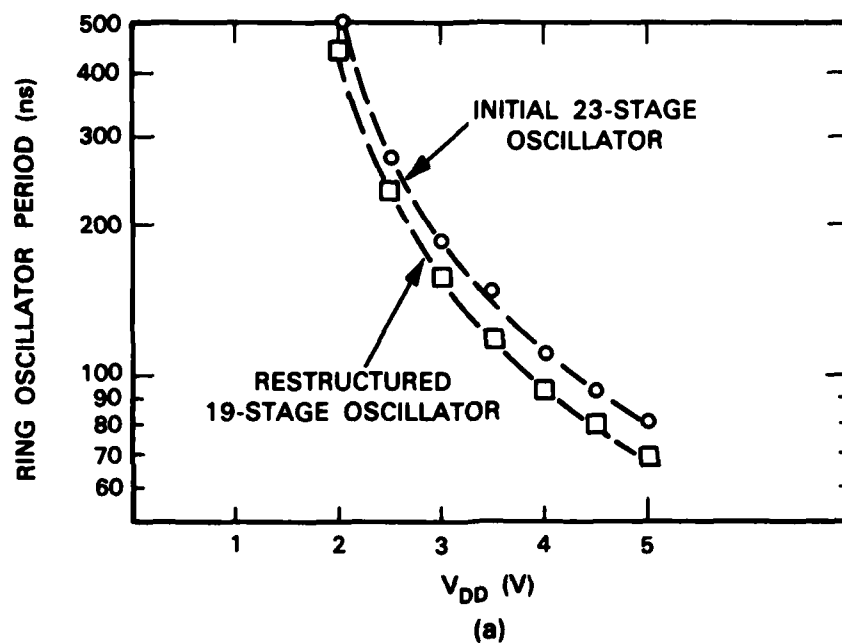


Figure 2-8. Electrical characteristics of ring oscillator circuits. (a) Oscillator period vs supply voltage for a ring oscillator before and after restructuring from 23 to 19 stages; (b) oscillator waveform of a 19-stage restructured oscillator.

132544-N-01

REFERENCES

1. D.K. Killinger, N. Menyuk, and W.E. DeFeo, Appl. Opt. 22, 682 (1983).
2. J.H. Shapiro, "Imaging and Target Detection with a Heterodyne-Reception Optical Radar," Project Report TST-24, Lincoln Laboratory (13 October 1978), DDC AD-A063767.
3. D.K. Killinger and N. Menyuk, Coherent Laser Radar Technical Digest, Optical Society of America Topical Meeting, Aspen, Colorado, 1-4 August 1983.
4. D.L. Spears, in *Optical and Laser Remote Sensing* (Springer-Verlag, New York, 1983), Vol. 39 in Optical Sciences Series.
5. M. Lanir and K.J. Riley, IEEE Trans. Electron Devices ED-29, 274 (1982).
6. S.R.J. Brueck, T.F. Deutsch, and D.E. Oates, Appl. Phys. Lett. 43, 157 (1983).
7. Solid State Research Report, Lincoln Laboratory, M.I.T. (1983:1), pp. 31-34, DTIC AD-A128894/3.
8. D.J. Ehrlich and J.Y. Tsao, to be published in *VLSI Electronics: Microstructure Science Vol. 7*, N.G. Einspruch, Ed. (Academic, New York); D.J. Ehrlich and J.Y. Tsao, to be published in J. Vac. Sci. Technol. November/December 1983.
9. J.Y. Tsao, D.J. Ehrlich, D.J. Silversmith, and R.W. Mountain, IEEE Electron Device Lett. EDL-3, 164 (1982).
10. D. Baurele, P. Irsigler, G. Leyendecker, H. Noll, and D. Wagner, Appl. Phys. Lett. 40, 819 (1982); D.J. Ehrlich, R.M. Osgood, Jr., and T.F. Deutsch, Appl. Phys. Lett. 39, 957 (1981); C.P. Christensen and K.M. Larkin, Appl. Phys. Lett. 32, 254 (1978).
11. J.Y. Tsao and D.J. Ehrlich, Appl. Phys. Lett. 43, 146 (1983).

3. MATERIALS RESEARCH

3.1 EFFICIENT AlGaAs SHALLOW-HOMOJUNCTION SOLAR CELLS

As a first step in the development of AlGaAs-Si tandem solar cells, shallow-homojunction cells have been fabricated in $\text{Al}_{0.2}\text{Ga}_{0.8}\text{As}$ epitaxial layers grown on single-crystal GaAs substrates by organometallic chemical vapor deposition (OMCVD). The one-sun conversion efficiency measured for the best cell was 12.9 percent at AM1.

The principal limitation on the efficiency of single-junction solar cells arises because the range of photon energies covered by the solar spectrum is too broad for efficient conversion by a single material. Potentially, a major increase in efficiency can be obtained by the use of tandem devices, in which cells with different energy gaps (E_g) are stacked vertically, with the cell facing the sun having the highest E_g . For two-cell devices, to obtain maximum overall efficiency the E_g values should be 1.75 to 1.80 eV for the top cell material and 1.0 to 1.1 eV for the bottom cell material.¹ With these values the maximum practical efficiency to be expected under one-sun, AM1 conditions is over 30 percent, compared with about 23 percent for single-junction cells. Such an increase in efficiency could make it advantageous to use tandem cells for both flat-plate and concentrator systems.

Because of its well-developed solar cell technology and low cost, single-crystal Si ($E_g = 1.1$ eV) is the material of choice for the bottom cell in a maximum-efficiency two-cell tandem structure. No material with a comparably developed technology is available for the top cell. At this time the most promising materials are the ternary III-V alloys $\text{Al}_x\text{Ga}_{1-x}\text{As}$ and $\text{GaAs}_{1-x}\text{P}_x$ with $x \approx 0.3$. With the objective of developing AlGaAs-Si tandem cells for efficient one-sun operation, we have initiated work on AlGaAs cells; they use the shallow-homojunction structure, without a window layer, that we have demonstrated for high-efficiency GaAs cells.²

The solar cells produced so far have been fabricated in $\text{Al}_{0.2}\text{Ga}_{0.8}\text{As}$ epitaxial layers that were grown on p^+ GaAs substrates. Growth was performed in a horizontal OMCVD reactor employing hydrogen at atmospheric pressure as the carrier gas and trimethylgallium, trimethylaluminum, and arsine as the source gases, with dimethyl zinc and hydrogen selenide used to dope the layers p- and n-type, respectively. The substrate temperature was 780°C, and the growth rate was 4.5 $\mu\text{m/h}$.

The solar cell structure, as shown schematically in Figure 3-1, consists of p^+ , p, and n^+ AlGaAs layers, together with a top n^+ GaAs layer used for the front contact. The fabrication techniques were similar to those used for GaAs cells.³ The back contact to the substrate was electroplated Au. The front contact bar and fingers, which were formed by patterning an evaporated Au film deposited on the n^+ GaAs layer, were protected during subsequent processing by a mask of plasma-deposited Si_3N_4 (Reference 3). The nonmetallized regions of the n^+ GaAs layer were etched off, and the exposed areas of the n^+ AlGaAs

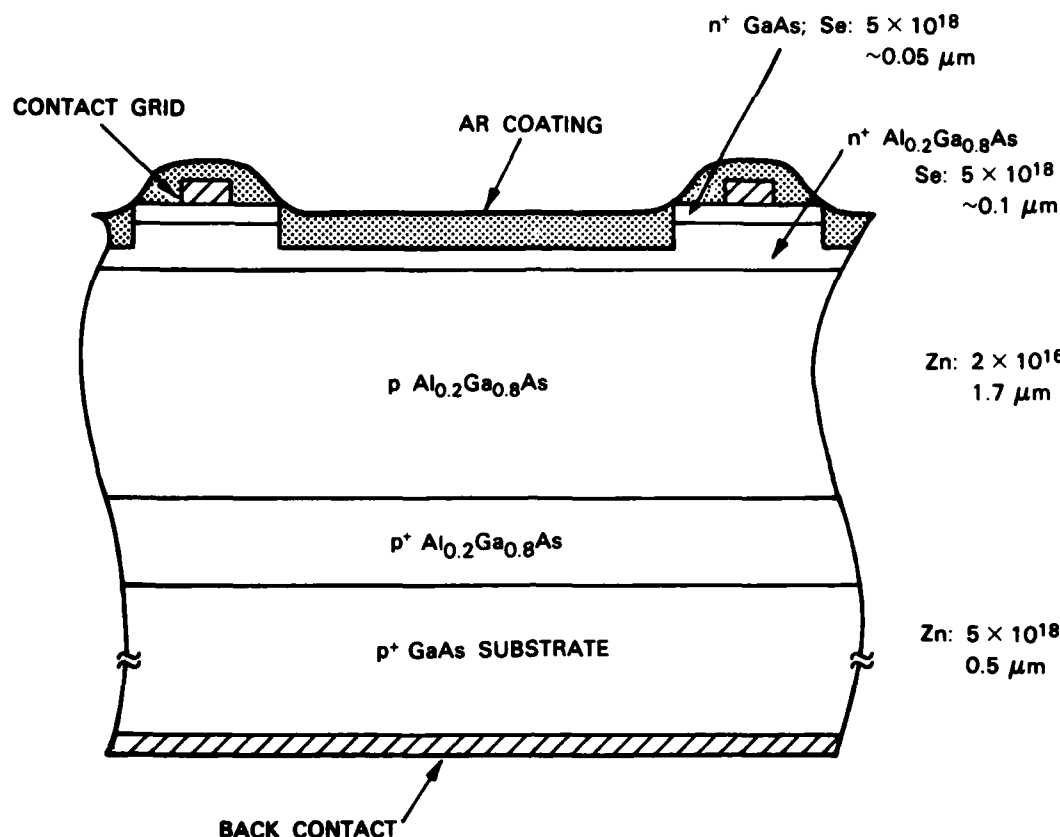


Figure 3-1. Schematic cross section of AlGaAs shallow-homojunction solar cell.

layer were then thinned to about 500 \AA by alternating anodic oxidation and oxide removal steps. The last of these steps was an anodization that formed an oxide layer with a refractive index of approximately 1.7 that served as an antireflection coating. Cell areas of 0.1 or 0.5 cm^2 were defined by conventional mesa techniques.

Figure 3-2 shows the current-voltage characteristic at 29°C for the best 0.1 cm^2 cell under simulated AMI conditions. A rooftop measurement was first made on the cell under nearly AMI conditions (95 mW/cm^2 , as determined by Si and GaAs calibration cells), giving a short-circuit current density J_{sc} of 14.6 mA/cm^2 and open-circuit voltage V_{oc} of 1.10 V. A current-voltage measurement was then made in the laboratory under illumination from a high-pressure Xe lamp filtered to give an AMI spectrum, with this simulator adjusted to give the same J_{sc} as the rooftop measurement. The value of V_{oc} was again 1.10 V. The curve of Figure 3-2 was obtained by normalizing the measured currents to J_{sc} of $(100/95) 14.6 = 15.4 \text{ mA/cm}^2$. The fill factor for this curve is 0.76, giving a one-sun efficiency of

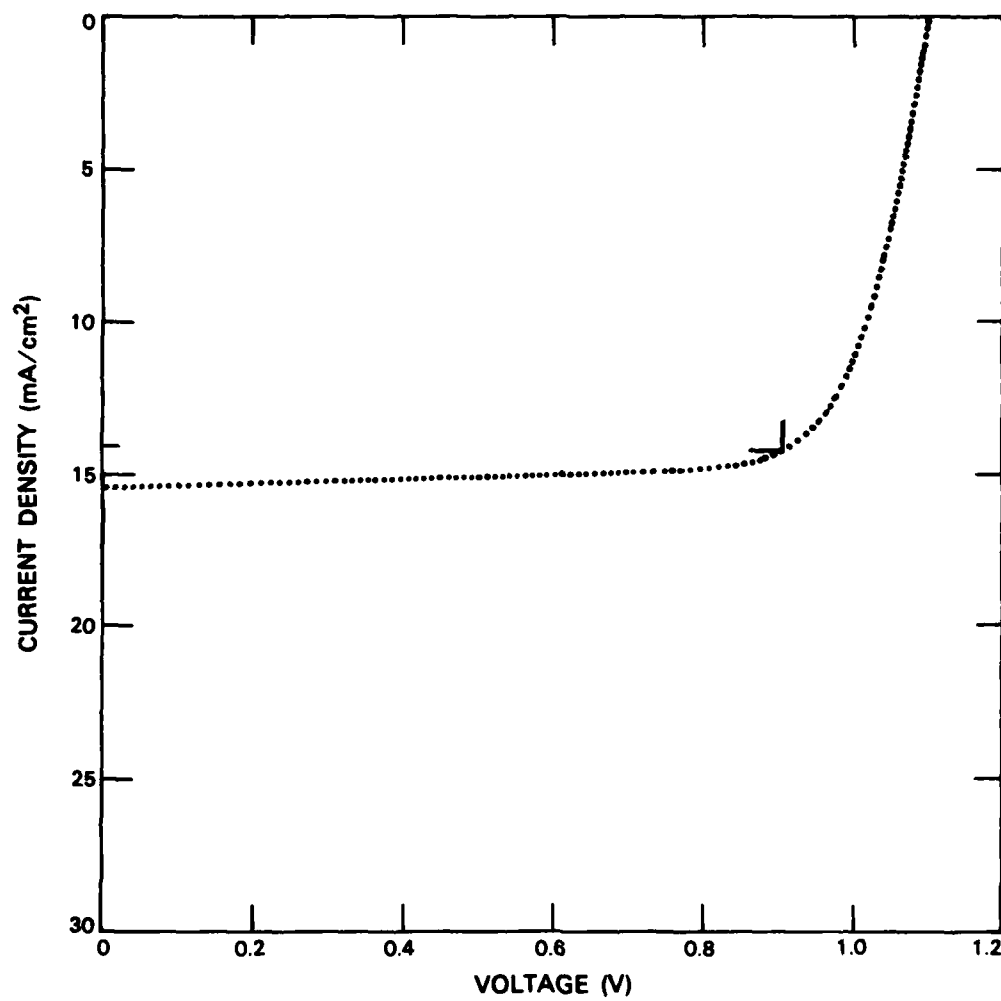


Figure 3-2. Current density as a function of voltage under simulated AM1 conditions for $\text{Al}_{0.2}\text{Ga}_{0.8}\text{As}$ cell with 12.9 percent conversion efficiency.

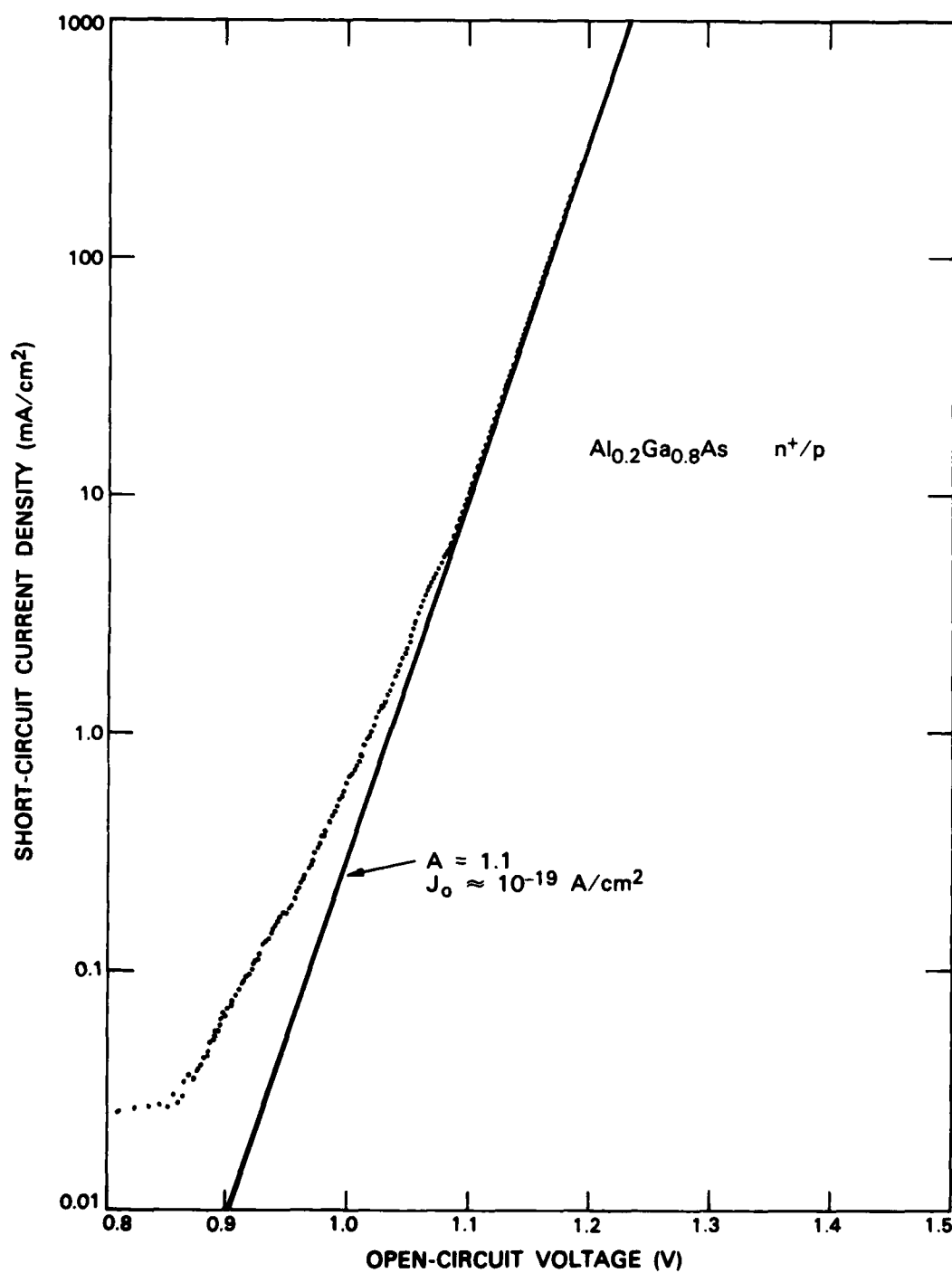


Figure 3-3. Short-circuit current density J_{sc} as a function of open-circuit voltage V_{oc} at different illumination levels for the cell of Figure 3-2.

12.9 percent at AM1. Similar results were obtained for a 0.5 cm² cell measured at 20°C, except that J_{sc} was 7 percent lower, giving a one-sun AM1 efficiency of 11.6 percent.

Figure 3-3 shows the dependence of J_{sc} on V_{oc} for the cell of Figure 3-2, as determined by pulsed measurements made at illumination levels up to about 20 suns with the cell mounted on a copper block maintained at 25°C. From the relationship⁴ $V_{oc} = A(kT/q) \ln[(J_{sc}/J_0) + 1]$, where k is Boltzmann's constant, T is the absolute temperature, and q is the electronic charge, we find that the diode factor $A = 1.1$ and the saturation current density $J_0 \approx 10^{-19}$ A/cm². These diode characteristics indicate that the n⁺/p junction is of high quality.

The external quantum efficiency of the cell of Figure 3-2 is plotted as a function of wavelength in Figure 3-4. The threshold at 0.75 μm (1.65 eV) corresponds to an alloy composition of Al_{0.2}Ga_{0.8}As, in agreement with the composition found by Auger measurements. The falloff in quantum efficiency between 0.6 and 0.7 μm is the principal factor limiting the cell photocurrent and conversion efficiency. This falloff suggests that the

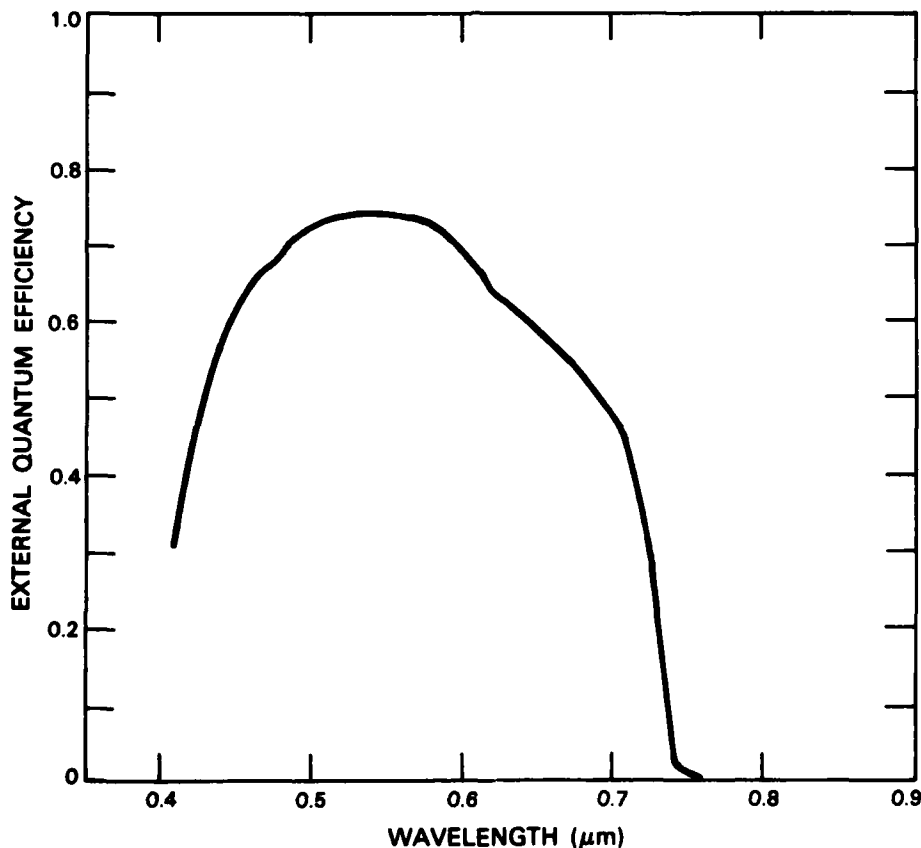


Figure 3-4. External quantum efficiency as a function of wavelength for the cell of Figure 3-2.

minority carrier diffusion length in the p layer is significantly less than the p-layer thickness and/or that this thickness is significantly less than the optical absorption length in the spectral region just above the absorption edge. In the short-wavelength region, where the absorption coefficients are greatest, the measured quantum efficiencies are equal to or better than those reported^{5,6} for AlGaAs heteroface cells with high-bandgap AlGaAs window layers. This result indicates that it should be possible for AlGaAs cells with the shallow-homojunction structure to achieve the conversion efficiencies required for high-performance AlGaAs-Si tandem devices.

R.P. Gale	R.L. Chapman
J.C.C. Fan	J.V. Pantano
G.W. Turner	

REFERENCES

1. J.C.C. Fan, B-Y. Tsaur, and B.J. Palm, in *Conference Record, 16th IEEE Photovoltaic Specialists Conference* (IEEE, New York, 1982), p. 692.
2. J.C.C. Fan, C.O. Bozler, and R.L. Chapman, *Appl. Phys. Lett.* **32**, 390 (1978).
3. Solid State Research Report, Lincoln Laboratory, M.I.T. (1983:3), p. 47; and G.W. Turner and M.K. Connors, *J. Electrochem. Soc.* (to be published).
4. M.P. Godleski, C.R. Baraona, and H.W. Brandhorst, Jr., in *Conference Record, 10th IEEE Photovoltaic Specialists Conference* (IEEE, New York, 1972), p. 40.
5. R.A. LaRue, P.G. Borden, M.J. Ludowise, P.E. Gregory, and W.T. Dietze, in *Conference Record, 16th IEEE Photovoltaic Specialists Conference* (IEEE, New York, 1982), p. 228.
6. C. Flores, *IEEE Electron Device Lett.* **EDL-4**, 96 (1983).

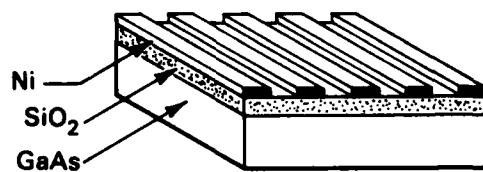
4. MICROELECTRONICS

4.1 FABRICATION OF ETCHED-GEOMETRY GaAs PERMEABLE-BASE TRANSISTORS

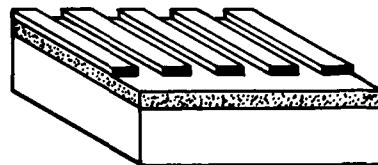
Etched-geometry GaAs permeable-base transistors (PBTs) with a $0.32\text{-}\mu\text{m}$ -period base grating and a $0.5\text{-}\mu\text{m}$ emitter-collector spacing have been fabricated. These PBTs differ from GaAs PBTs previously reported¹ in that the growth of GaAs over a submicrometer-periodicity metal base grating, which is a formidable technological problem, is not required. In this respect these PBTs are similar to GaAs vertical field-effect transistors previously reported.² However, in the devices reported here, the base grating dimensions are approximately six times smaller. This reduces intrinsic device capacitances for comparable doping levels without substantially affecting the transconductance, thus increasing high-frequency performance.

The fabrication of etched-geometry GaAs PBTs is outlined in Figure 4-1. First, an $\text{AsCl}_3\text{-GaAs-H}_2$ vapor phase epitaxy system is used to grow a $0.5\text{-}\mu\text{m}$ -thick n-GaAs layer on a (100) $n^+\text{-GaAs}$ substrate. Next, $0.1\text{ }\mu\text{m}$ of CVD SiO_2 is deposited to protect the GaAs surface during subsequent processing. X-ray lithography and lift-off are used to define a $0.32\text{-}\mu\text{m}$ -period Ni grating on the SiO_2 surface. Ni is then selectively removed by HCl etching in regions which will eventually be shorting bars for the base grating and selectively deposited in regions which eventually will be shorting bars for the collector grating. Since the dimensions of the shorting bars are relatively large ($>10\text{ }\mu\text{m}$), standard photolithography can be used for these steps. The patterned Ni serves as an etch mask for reactive-ion etching of the SiO_2 in CF_4 . Since the etch rate of GaAs is much lower than that for SiO_2 , the etching can be controllably stopped just below the $\text{SiO}_2\text{-GaAs}$ interface. Ion-beam-assisted etching is then used to etch vertical grooves in the GaAs. The active region of the device at this point in the fabrication sequence is shown in the scanning-electron micrographs (SEMs) of Figure 4-2. The collector and base Schottky-barrier contacts are formed simultaneously with a single $\sim 300\text{-}\text{\AA}$ -thick Al evaporation. The active regions of these devices are isolated by proton bombardment, and extra Al is evaporated in the patterned regions to form contact pads to the collector and base shorting bars. The completed device is shown schematically in Figure 4-3 and in the SEM of Figure 4-4.

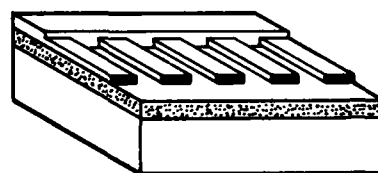
Etched-geometry GaAs PBTs exhibit triode-like three-terminal I-V characteristics, as shown in Figure 4-5. This is consistent with the existence of a barrier on the collector side of the base due to Fermi-level pinning at the exposed GaAs surfaces. A maximum frequency of oscillation, f_{max} , of 16 GHz and a small signal, short-circuit unity-current-gain frequency, f_T , of 13 GHz have been determined from S-parameter measurements from 2 to 18 GHz. Numerical simulations³ indicate that process optimization of the present structure, such as a modified doping profile to reduce the problem of Fermi-level pinning, will result



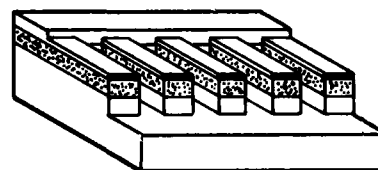
DEFINE SUBMICROMETER-PERIOD
GRATING Ni ETCH MASK BY
X-RAY LITHOGRAPHY AND LIFT-OFF



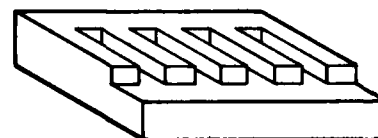
SELECTIVELY REMOVE Ni



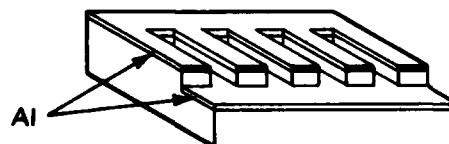
SELECTIVELY DEPOSIT Ni



RIE SiO_2 AND IBAE GaAs



REMOVE ETCH MASK



EVAPORATE ALUMINUM
FOR SCHOTTKY CONTACT
COLLECTOR AND BASE

Figure 4-1. Fabrication sequence for etched-geometry GaAs PBTs.

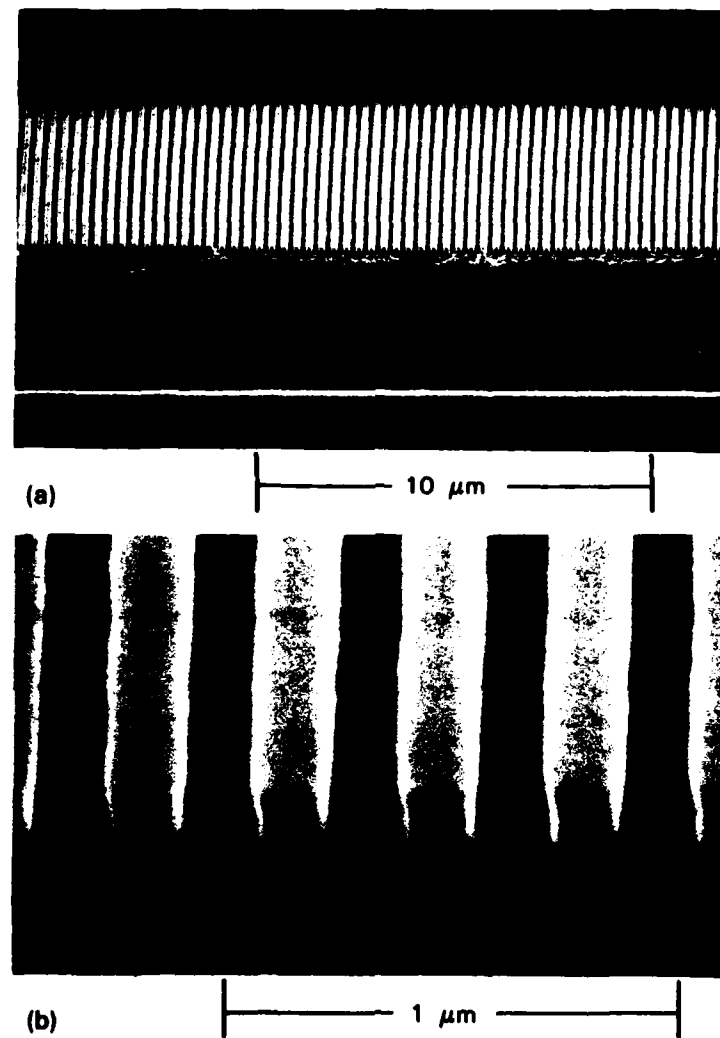


Figure 4-2. SEMs of the etched GaAs grating which forms the device active region.

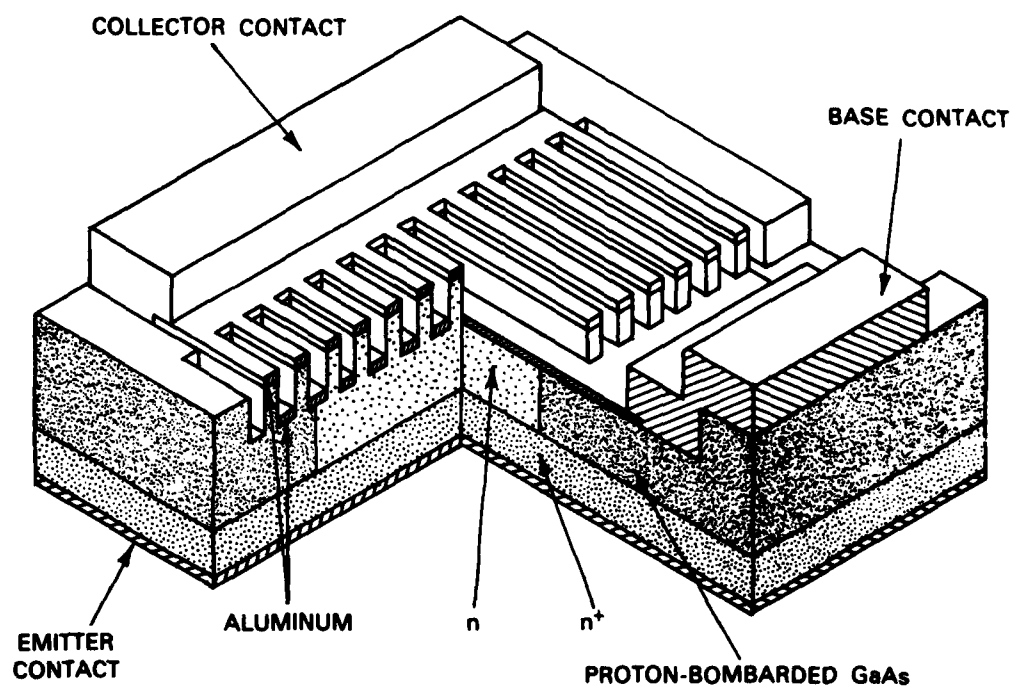


Figure 4-3. Schematic diagram of an etched-geometry GaAs PBT.

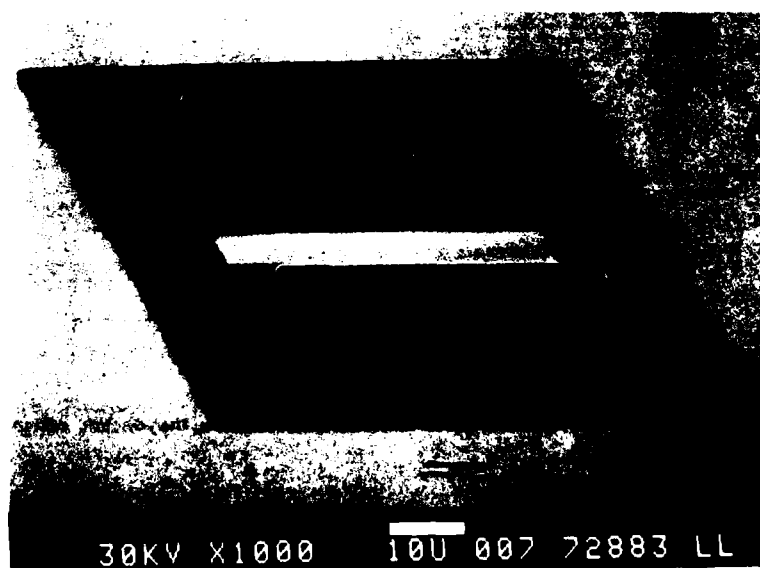


Figure 4-4. SEM of a completed etched-geometry GaAs PBT.

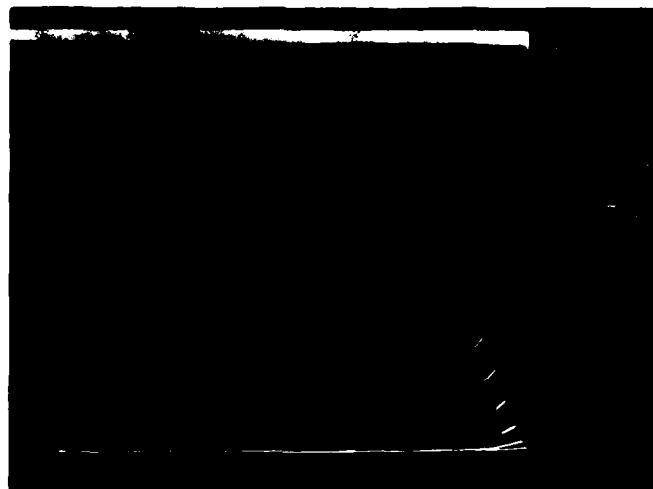


Figure 4-5. Typical three-terminal current-voltage characteristics of an etched-geometry GaAs PBT. The top trace is at a +0.6-V base-to-emitter bias and the steps are 0.2 V.

in high-frequency etched-geometry GaAs PBT operation with an $f_T > 40$ GHz. This f_T is comparable to that predicted for an overgrown GaAs PBT of similar dimensions.

B.A. Vojak	A.R. Calawa
G.A. Lincoln	M.W. Geis
D.D. Rathman	R.W. McClelland
D.C. Flanders	

4.2 NITROCELLULOSE AS A SELF-DEVELOPING RESIST WITH SUBMICROMETER RESOLUTION AND PROCESSING STABILITY

Self-developing resists are a class of materials which volatilize during exposure, and therefore require no development step. Several materials exhibit this property when exposed to the appropriate radiation.⁴⁻¹¹ Recently, self-development has been demonstrated on a submicrometer scale with nitrocellulose.^{4,5} When nitrocellulose is impacted with heavy ions, e.g., Ar^+ or Xe^+ , or exposed to laser radiation of sufficient energy, microcombustion occurs which ablates the surface, giving the self-developing characteristics. However, when this material is exposed to light ions, electrons, or a low energy flux of UV radiation ($< 2 \text{ mW/cm}^2$), it decomposes forming both volatile and nonvolatile products. The nonvolatile products are believed responsible for the processing stability of this self-developing resist.

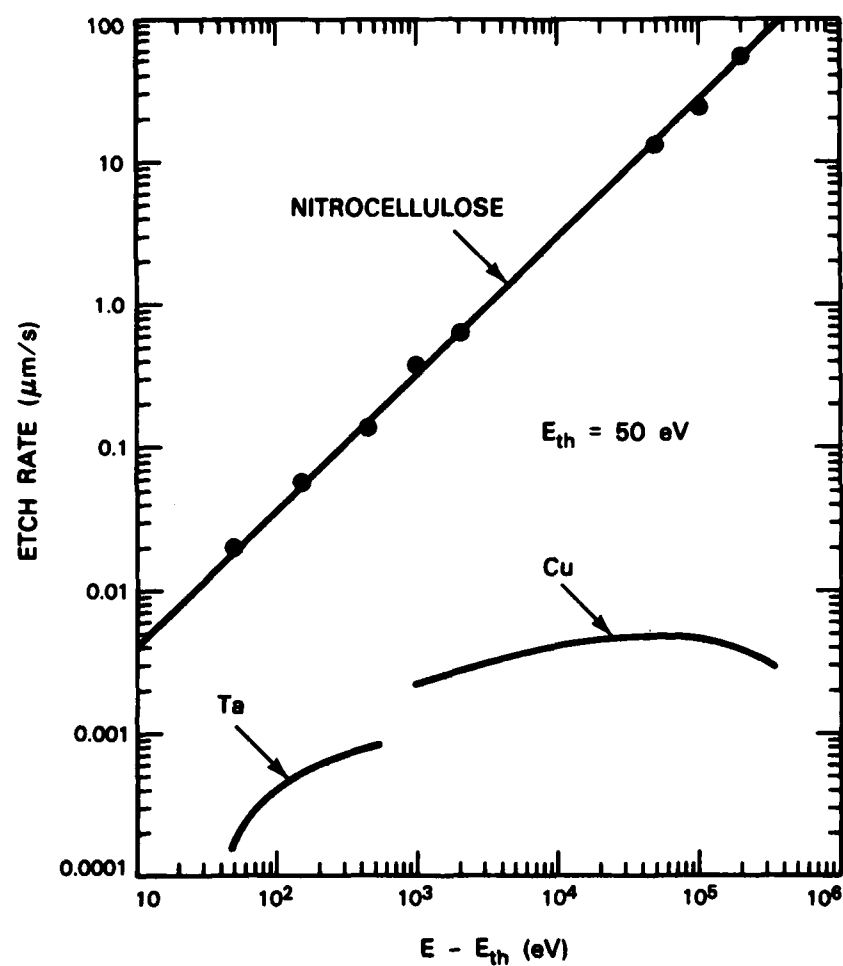


Figure 4-6. Etch rate of nitrocellulose as a function of Ar^+ energy minus a threshold energy of 50 eV. The data are normalized to a beam current of 1 mA cm^{-2} . The sputtering rates of tantalum and copper, obtained from the data of References 12 and 13, are shown for comparison.

128196-N-01

Experiments were performed to study the characteristics of nitrocellulose when exposed to an Ar^+ beam. Figure 4-6 shows the self-development rate as a function of the ion energy. The development sensitivity of 190 eV nm^{-3} is linear with respect to ion energy beyond a threshold energy of 50 eV, over nearly four decades variation in ion energy. The sputtering rates for tantalum and copper, obtained from the literature,^{12,13} are shown for comparison. The different dependence of etch rate on ion energy indicates that nitrocellulose does not develop by sputtering. The development rate is consistently two to four orders of magnitude higher than the sputtering rate of most materials. Figure 4-7 shows a scanning-electron micrograph of a grating with a 320-nm period made by ion beam exposing $0.6 \mu\text{m}$ of nitrocellulose through a SiN_x stencil mask;¹⁴ the aspect ratio is $\sim 7:1$. The volatile decomposition products produced during ion beam exposure are shown in Figure 4-8. The major constituents, as determined by a quadrupole mass spectrometer, are water, nitrogen, carbon monoxide, nitric oxide, and carbon dioxide.

The stability of nitrocellulose to dry processing has also been characterized. Most dry etching processes require the use of a plasma of reactive gas. These plasmas consist of electrons, light ions, and UV radiation, all of which cause nitrocellulose to develop slowly and form nonvolatile residues.⁴ Figure 4-9 shows a comparison of reactive-ion etching rates of nitrocellulose, SiO_2 , and ferrocene-doped nitrocellulose using CHF_3 as the reactive gas. The reactive-ion etching rates for nitrocellulose are about two orders of magnitude lower than those obtained by argon ions with energies in electron volts equivalent to the target voltage, as shown in Figure 4-6. It is difficult to make direct comparisons since the ion flux in



Figure 4-7. SEM of a grating pattern in a $0.6\text{-}\mu\text{m}$ -thick nitrocellulose film on a silicon wafer. The sample was exposed to a beam of 500-eV Ar^+ at a current density of 0.25 mA cm^{-2} for 40 s. The SiN_x stencil mask used for this exposure consisted of a 320-nm grating with a crossmember every $3.8 \mu\text{m}$ to strengthen the mask. Two shadows of the crossmembers can be seen in the nitrocellulose.

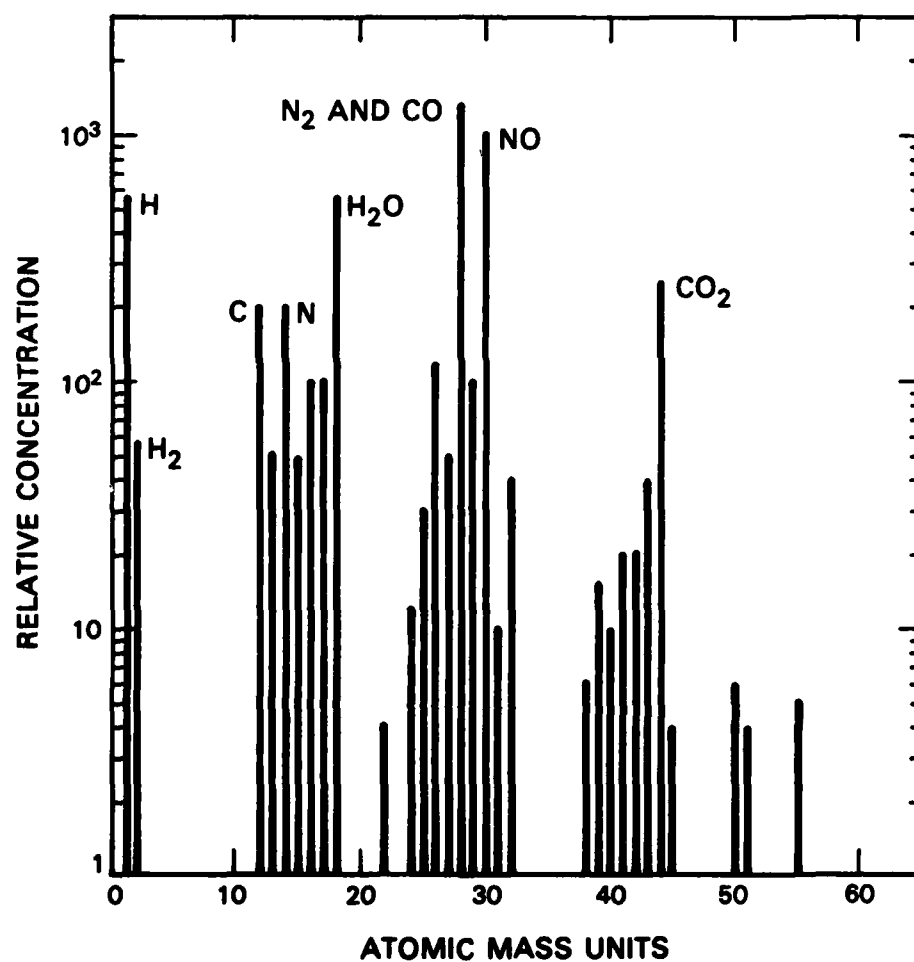


Figure 4-8. Volatile decomposition products of nitrocellulose when exposed to a beam of 2-keV Xe^+ at 1 mA cm^{-2} . The products were detected by a quadrupole mass spectrometer and the background gas spectrum was subtracted from the data.

128351-N-01

reactive-ion etching is not known. Although the reactive-ion etching rate of nitrocellulose is surprisingly low, it is still twice that of SiO_2 and of limited processing value. As shown in Figure 4-9, the addition of 10 wt.% ferrocene, a volatile metal complex, reduces the etching rate of nitrocellulose by a factor of 4 to about half that of SiO_2 . The development rate of the doped resist by 2 keV Xe^+ is reduced by more than a factor of 20 compared with the undoped resist, but the development rate obtained with the ArF laser is unaffected.

Nitrocellulose has been characterized as a self-developing resist with resolution <100 nm and processing stability acceptable for some applications.

M.W. Geis
J.N. Randall
T.F. Deutsch

N.N. Efremow
J.P. Donnelly
J.D. Woodhouse

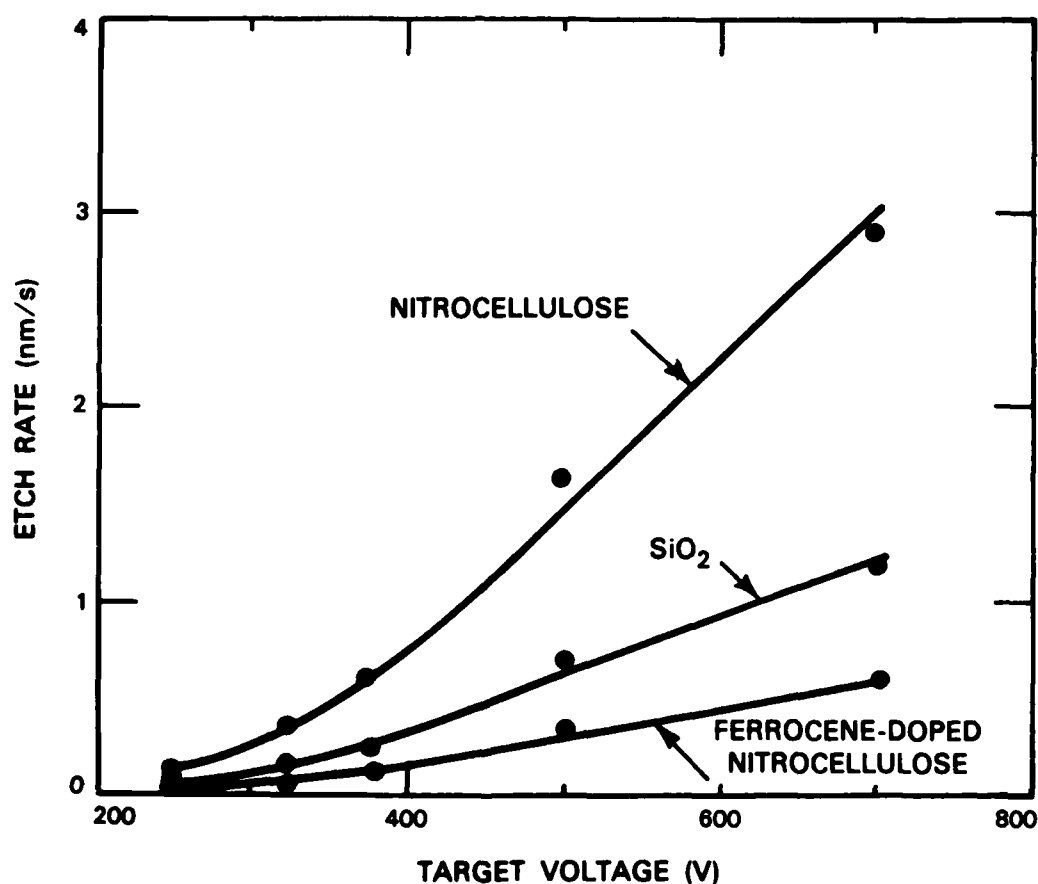


Figure 4-9. Reactive-ion etching rate of nitrocellulose, SiO_2 , and ferrocene-doped nitrocellulose. The etch gas was CHF_3 at a pressure of 25 Torr and a flow rate of 45 sccm. The samples were placed on a quartz plate which covered the water-cooled powered electrode.

4.3 EFFECT OF BASE GEOMETRY ON Si PBT DEVICE PERFORMANCE

In this study some experimental device results are compared with two-dimensional numerical simulations of Si permeable-base transistors (PBTs).¹⁵ Both the simulations and experimental devices indicate that small variations in the metal-semiconductor contact area of the base fingers, such as those shown in Figure 4-10, can lead to substantial deviations in important device parameters such as transconductance, G_m , threshold voltage, V_T , and device intrinsic input capacitance, C_{in} . Variations in base-metal linewidth and thickness yield similar effects.

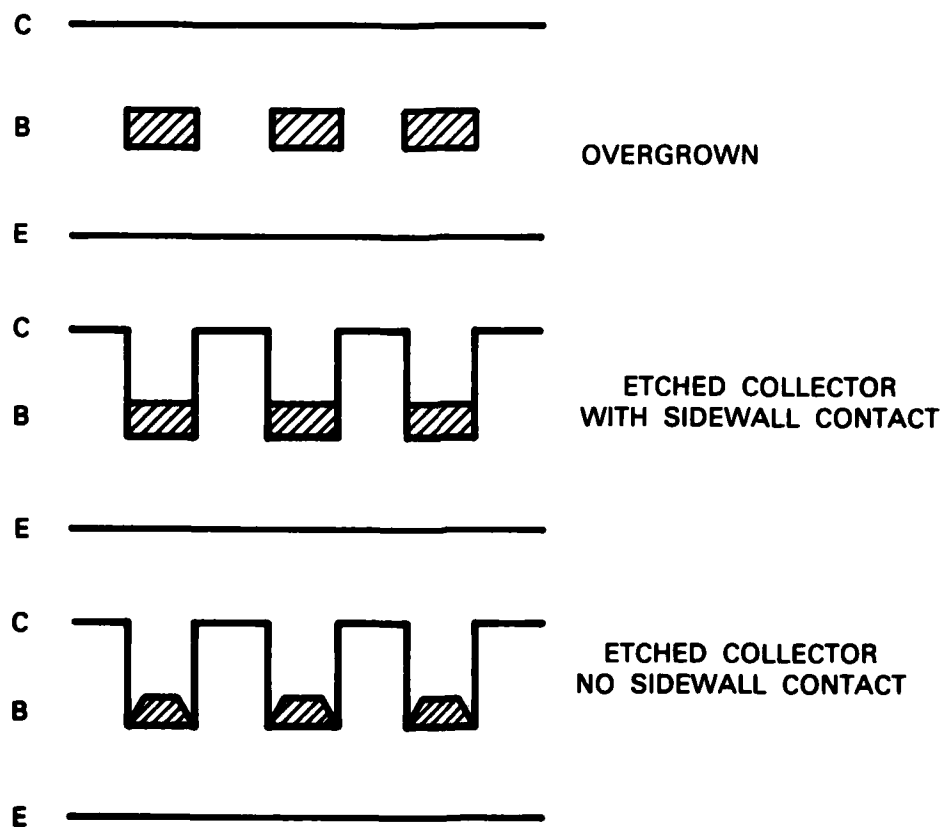


Figure 4-10. Comparison of three base geometry configurations for the Si PBT. The differences are in the metal-semiconductor contact area in the base region.

The two-dimensional numerical simulations used to evaluate the device parameters for the three base-metal configurations shown in Figure 4-10 have been described in detail elsewhere.¹⁶ For the configurations shown, base-metal periodicity (320 nm), semiconductor doping ($4 \times 10^{16} \text{ cm}^{-3}$) and base-metal thickness (40 nm) were kept constant. The results are summarized in Figures 4-11 through 4-13. Figure 4-11 shows the collector current density, J_c , as a function of base-to-emitter voltage at a fixed collector-to-emitter voltage ($V_{CE} = 1.0 \text{ V}$) for each of the device configurations. Note the relatively large variations in J_c with V_{BE} for both overgrown and etched collector with sidewall contact configurations. The etched collector without sidewall contact shows little variation in J_c , indicative of low transconductance or poor base control.

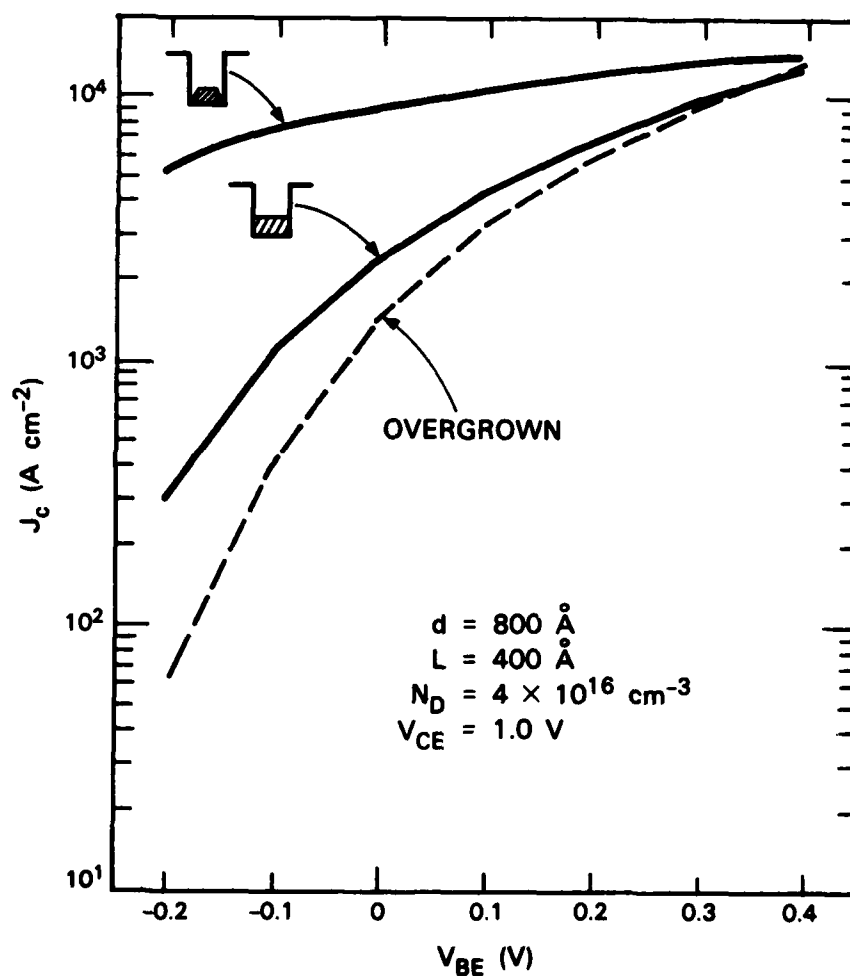


Figure 4-11. Comparison of J_c vs V_{BE} for the overgrown Si PBT, the etched collector structure with sidewall contact, and the etched collector structure without sidewall contact at $V_{CE} = 1.0 \text{ V}$. L is base-metal thickness and d is spacing between adjacent base finders.

Figure 4-12 shows the small-signal, short-circuit unity-current-gain frequency, f_T , as a function of V_{BE} for the three device configurations. Although the bias dependence of f_T is different for the three devices, the maximum value of f_T is nearly constant. This is because the ratio of G_m to C_{in} is approximately equal for the three configurations. The optimum bias conditions for f_T , however, are shifted toward lower base-to-emitter voltages for the geometry which tends toward diminished base control.

The important device parameters are summarized in Figure 4-13. Note that the configuration with the largest transconductance (overgrown) also has the largest capacitance. In addition, the threshold or turnoff voltage, V_T , is also the largest. The conclusion is straightforward: the greater the base-metal-semiconductor contact area, the greater the base control, as indicated by high G_m and V_T . However, the increase in base control is at the expense of increased capacitance, leaving the intrinsic f_T invariant.

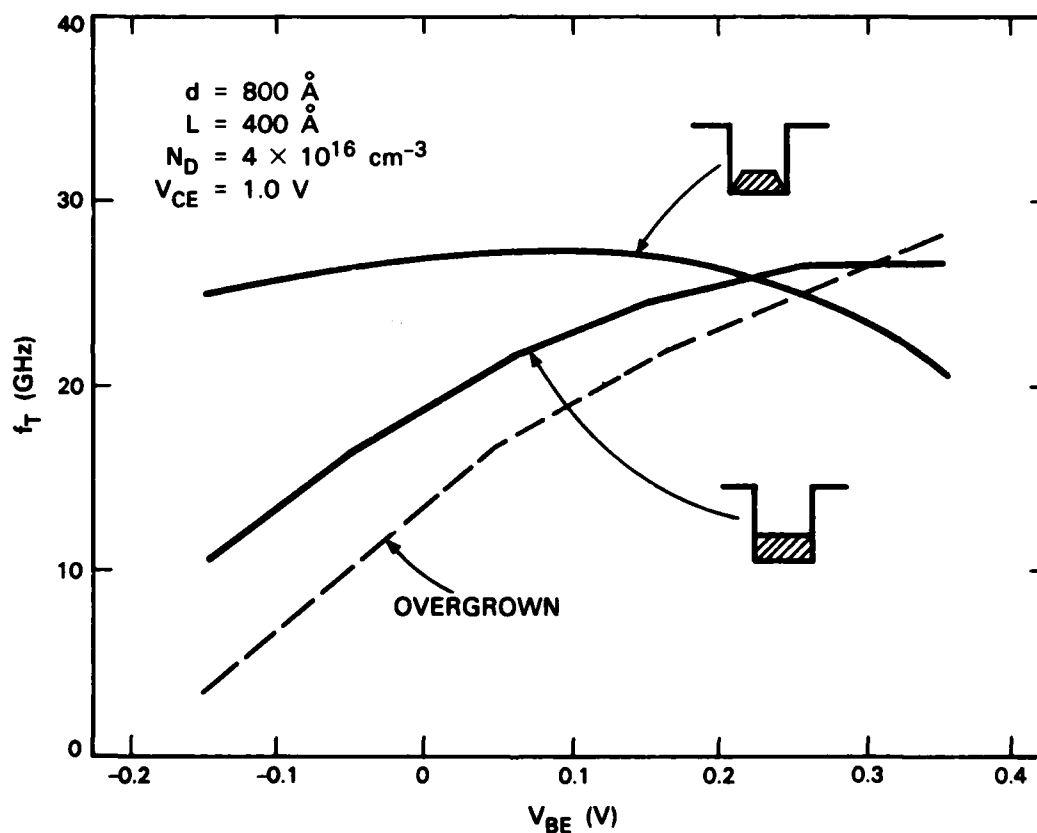
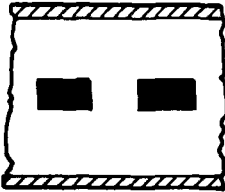
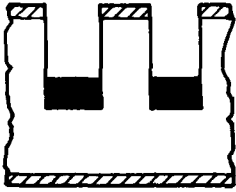
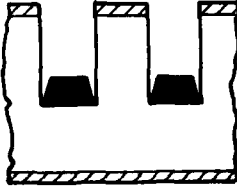


Figure 4-12. Unity short-circuit current-gain frequency, f_T , as a function of V_{BE} for the same devices as Figure 4-11.

Two etched-collector Si PBT devices have been fabricated. The submicrometer-period U-groove active region was formed by a combination of X-ray lithography and reactive-ion etching. The details of the fabrication procedure have been described elsewhere.¹⁵ Both devices have $40 \times 8\text{-}\mu\text{m}$ active areas, 320-nm-periodicity base gratings and $4 \times 10^{16}\text{ cm}^{-3}$ doping. The important difference is the base-metal configuration at the groove bottoms.

Figures 4-14 and 4-15 are scanning-electron micrographs showing the base-metal regions of the two devices. In addition, the corresponding three-terminal I-V characteristics are displayed. Note that for the device of Figure 4-14 the W base metal is cleanly separated from the groove sidewalls while the device of Figure 4-15 appears to have at least partial contact between metal and sidewall. The differences in the three-terminal characteristics of the two devices, however, are even more striking. The device of Figure 4-15 which has sidewall contact has substantially higher transconductance than the device of Figure 4-14. In addition, the threshold voltage for the device of Figure 4-15 is approximately -0.8 V for the device without sidewall contact. We have also verified experimentally that the device capacitance is approximately 20 percent higher for the device of Figure 4-15. The experimental results thus exhibit the trends predicted by the simulations.

			
	OVERGROWN	ETCHED GEOMETRY	NO SIDEWALL CONTACT
$V_T\text{ (V)}$	-0.2	-0.3	-1.0
$\max f_T\text{ (GHz)}$	28	27	27
$G_m _{\max f_T}\text{ (mS)}$	147	130	75
$C_{in} _{\max f_T}\text{ (pF)}$	0.85	0.77	0.44

($V_{CE} = 1.7\text{ V}$, V_{BE} chosen for $\max f_T$, $10 \times 40\text{ }\mu\text{m}^2$ area)

Figure 4-13. Comparison of important parameters for the three device configurations described in Figures 4-10 through 4-12.

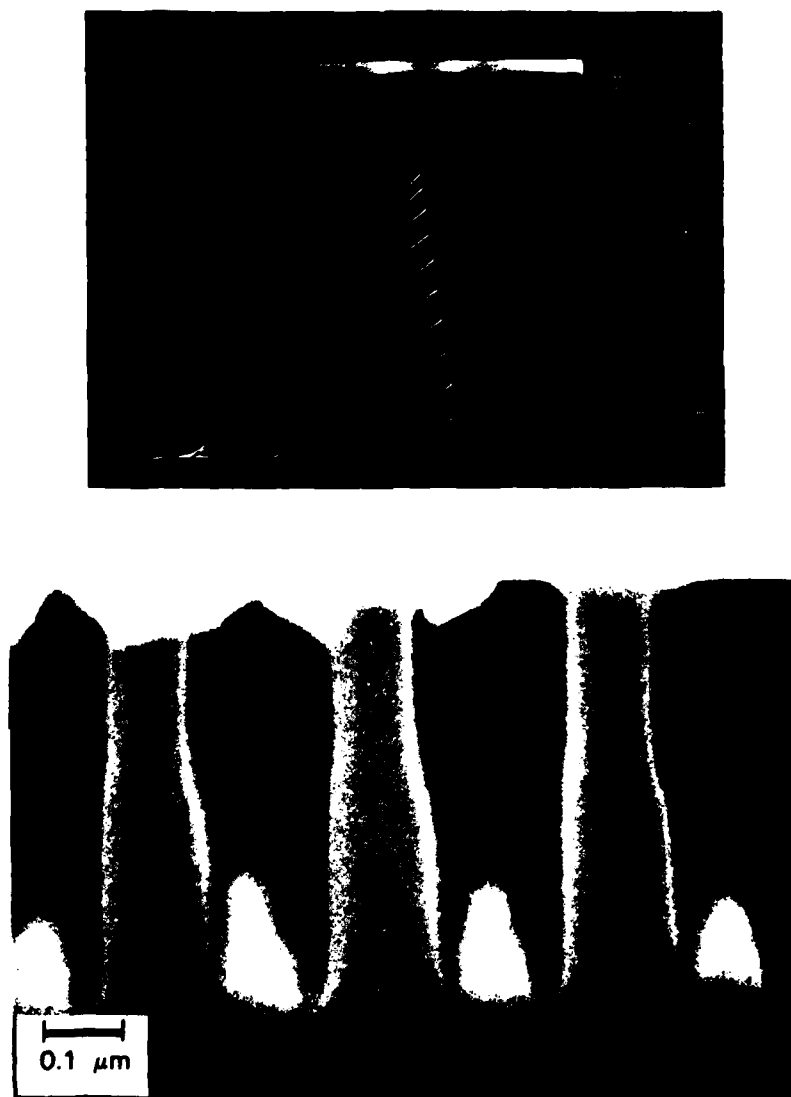


Figure 4-14. SEM of the base region of a Si PBT, where the W base metal is separated from the Si sidewall. In the corresponding I-V characteristics shown above, $V_{BE} = +0.4$ for the top curve.

131246-R

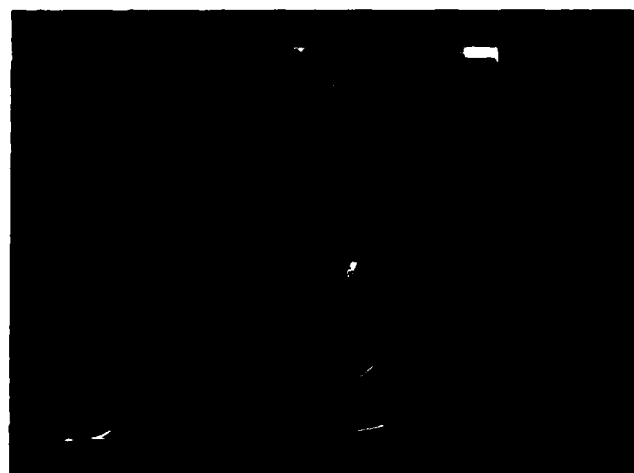


Figure 4-15. SEM of the base region of a Si PBT in which the base metal appears to be in partial contact with the Si sidewall. In the corresponding I-V characteristics shown above, $V_{BE} = +0.4$ for the top curve.

In the experimental devices, f_T is limited to between 20 and 40 percent of the predicted value due to parasitic capacitances (e.g., base pad capacitance). Optimization of f_T is therefore accomplished by using the base-metal configuration that maximizes both G_m and intrinsic device capacitance. For the above devices, where the parasitic capacitances are roughly equivalent, the device with sidewall contact had an f_T equal to 10 GHz compared with 5.5 GHz for the device without sidewall contact. Future efforts will be made both to maximize sidewall contact in the base region adjacent to the conducting channel and to minimize parasitic capacitances.

D.D. Rathman

B.A. Vojak

J.A. Burns (Group 23)

L.A. Stern

S.M. Cabral

REFERENCES

1. C.O. Bozler and G.D. Alley, IEEE Trans. Electron Devices **ED-27**, 1128 (1980).
2. E. Kohn, U. Mishra, and L.F. Eastman, IEEE Electron Device Lett. **EDL-4**, 125 (1983).
3. M. Osman, D.H. Navon, T.W. Tang, and L. Sha, to be published in IEEE Trans. Electron Devices.
4. M.W. Geis, J.N. Randall, T.F. Deutsch, P.D. DeGraff, K.E. Krohn, and L.A. Stern, Appl. Phys. Lett. **43**, 74 (1983).
5. T.F. Deutsch and M.W. Geis, J. Appl. Phys. **54**, 7201 (1983).
6. M. Isaacson and A. Murray, J. Vac. Sci. Technol. **19**, 1117 (1981).
7. N. Ueno, S. Konishi, K. Tanimoto, and K. Sugita, Jpn. J. Appl. Phys. **20**, L709 (1981).
8. R. Srinivasan and V. Mayne-Banton, Appl. Phys. Lett. **41**, 576 (1982).
9. J.E. Andrew, P.E. Dyer, D. Foster, and Ph.H. Key, to be published in Appl. Phys. Lett.
10. K.A. Valiev, L.K. Velikov, S.D. Dushenkov, A.Y. Mitrofanov, and A.M. Prokhorov, Sov. Tech. Phys. Lett. **8**, 22 (1978).
11. M.J. Bowden, CRC Crit. Rev. Solid State Mater. Sci. **8**, 223 (1978).
12. N. Laegreid and G.K. Wehner, J. Appl. Phys. **32**, 365 (1961).
13. A.L. Southern, W.R. Willis, and M.T. Robinson, J. Appl. Phys. **34**, 153 (1963); also M.I. Guseva, Sov. Phys.-Solid State **1**, 1410 (1960); and G. Dudd and A. Scharmann, Z. Phys. **192**, 284 (1966).
14. J.N. Randall, D.C. Flanders, N.P. Economou, J.P. Donnelly, and E.I. Bromley, Appl. Phys. Lett. **42**, 457 (1983).
15. D.D. Rathman, N.P. Economou, D.J. Silversmith, R.W. Mountain, and S.M. Cabral, Proc. IEEE Intl. Electron Devices Mtg., San Francisco, 13-15 December 1982, p. 650.
16. B.A. Vojak and G.D. Alley, IEEE Trans. Electron Devices **ED-30**, 877 (1983).

5. ANALOG DEVICE TECHNOLOGY

5.1 GAUSSIAN CONVOLUTION OF IMAGES STORED IN A CHARGE-COUPLED DEVICE

This report describes the experimental demonstration of a new method for producing the convolution with a Gaussian function of an optical image stored in a charge-coupled device (CCD) array. Such Gaussian convolution operations are the time-consuming steps in the difference-of-Gaussians (DOG) procedure¹ employed in artificial intelligence algorithms for the detection and localization of the edges of objects in an image. The method described here can produce such convolutions for arbitrarily large fields of view in a time less than that required to detect the original image.

The method is based on the fact that Gaussian convolution provides the mathematical description of the physical process of diffusion. Since diffusion results from a large number of small intermixing events, what is required is a CCD clocking technique that allows a controlled mixing of adjacent charge packets in the CCD. To accomplish this, the CCD structure needs the following elements: (a) pixel wells to hold the charge packets representing the image intensities, (b) mixing wells between pixel wells to hold the charge to be exchanged between adjacent pixel wells, and (c) transfer wells that can isolate mixing wells from or connect mixing wells to their neighboring pixel wells.

One example of such a structure is a one-dimensional four-phase CCD, as shown in Figure 5-1. The phase-1 wells serve as pixel wells, the phase-3 wells as mixing wells, and the phase-2 and phase-4 wells as transfer wells. Figure 5-2 shows the clocking technique that can be used to generate Gaussian convolution. In an ideal case, the mixing wells would have infinitesimal areas and the number of mixing cycles would approach infinity. The product of the mixing fraction and the number of mixing cycles would determine the width of the Gaussian function generated. In practice the area of the mixing well can be large and the number of mixing cycles small. A set of Gaussian kernel functions with discrete width parameters can be generated corresponding to the integral numbers of mixing cycles (including zero).

The results reported here were obtained using a standard four-phase CCD in which the mixing wells and pixel wells have the same area. Figure 5-3 shows the expected evolution of a single, unit-intensity pixel through two mixing cycles. After each cycle the charge distribution represents a binomial approximation to a Gaussian function of a specific width. For an arbitrary initial distribution of charge packets, the result is the convolution of that distribution with the Gaussian kernel function.

Figure 5-4 shows photographs of the output from a 32-stage CCD containing an initial charge pattern of eight full wells after various numbers of mixing cycles from 0 to 16. The sizes of the charge packets were measured from the photographs and compared to the results expected; the agreement was well within the measurement accuracy. Table 5-1 shows a comparison between the values measured from the original photographs in Figure 5-4, the

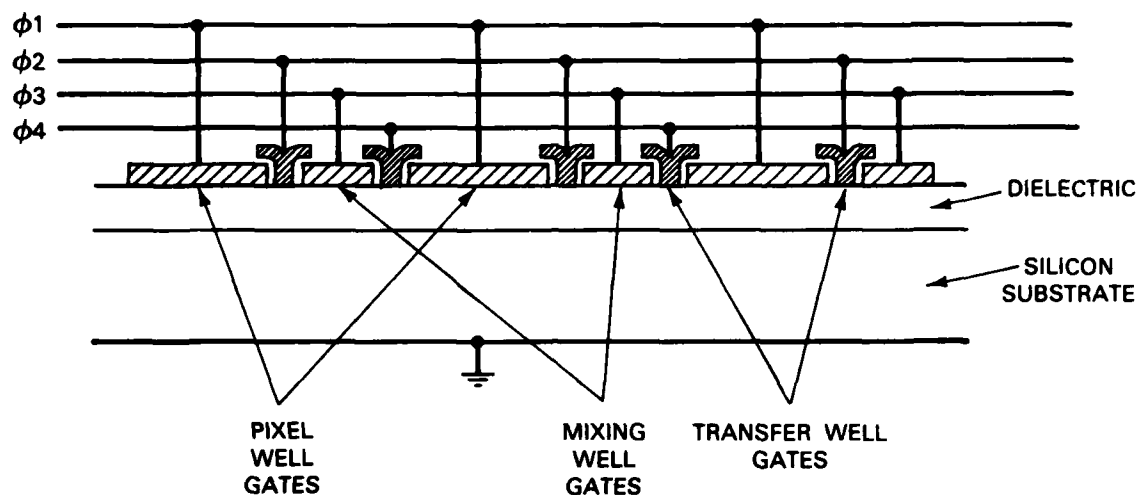


Figure 5-1. Example of a CCD structure in which Gaussian convolution can be carried out.

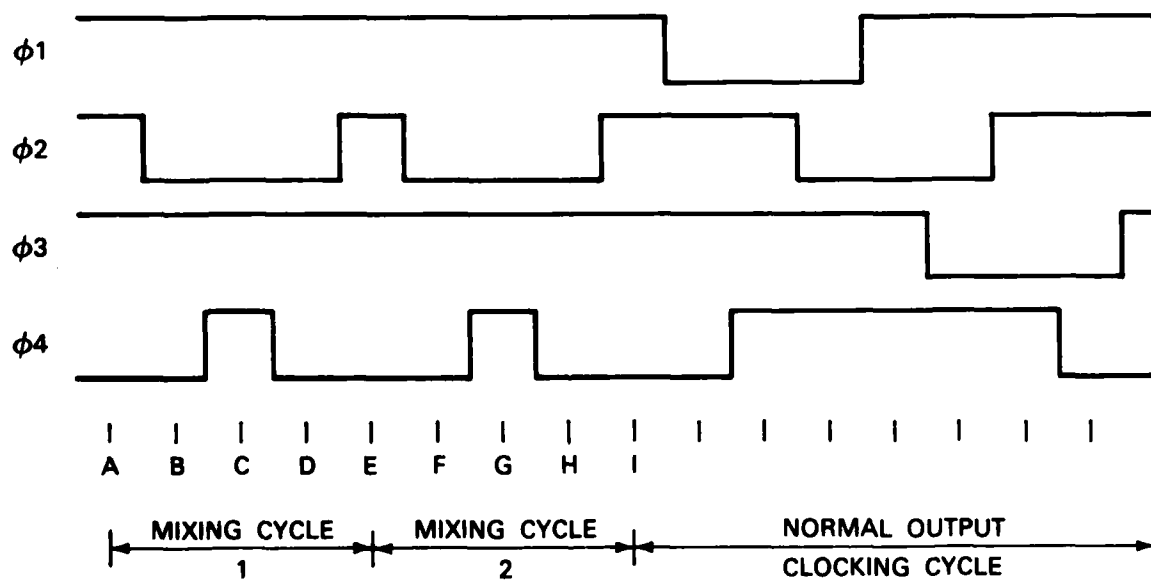


Figure 5-2. Clocking waveforms used to produce Gaussian convolution of a signal stored in a CCD. The A-I designations of time are keyed to the charge mixing sequence in Figure 5-3.

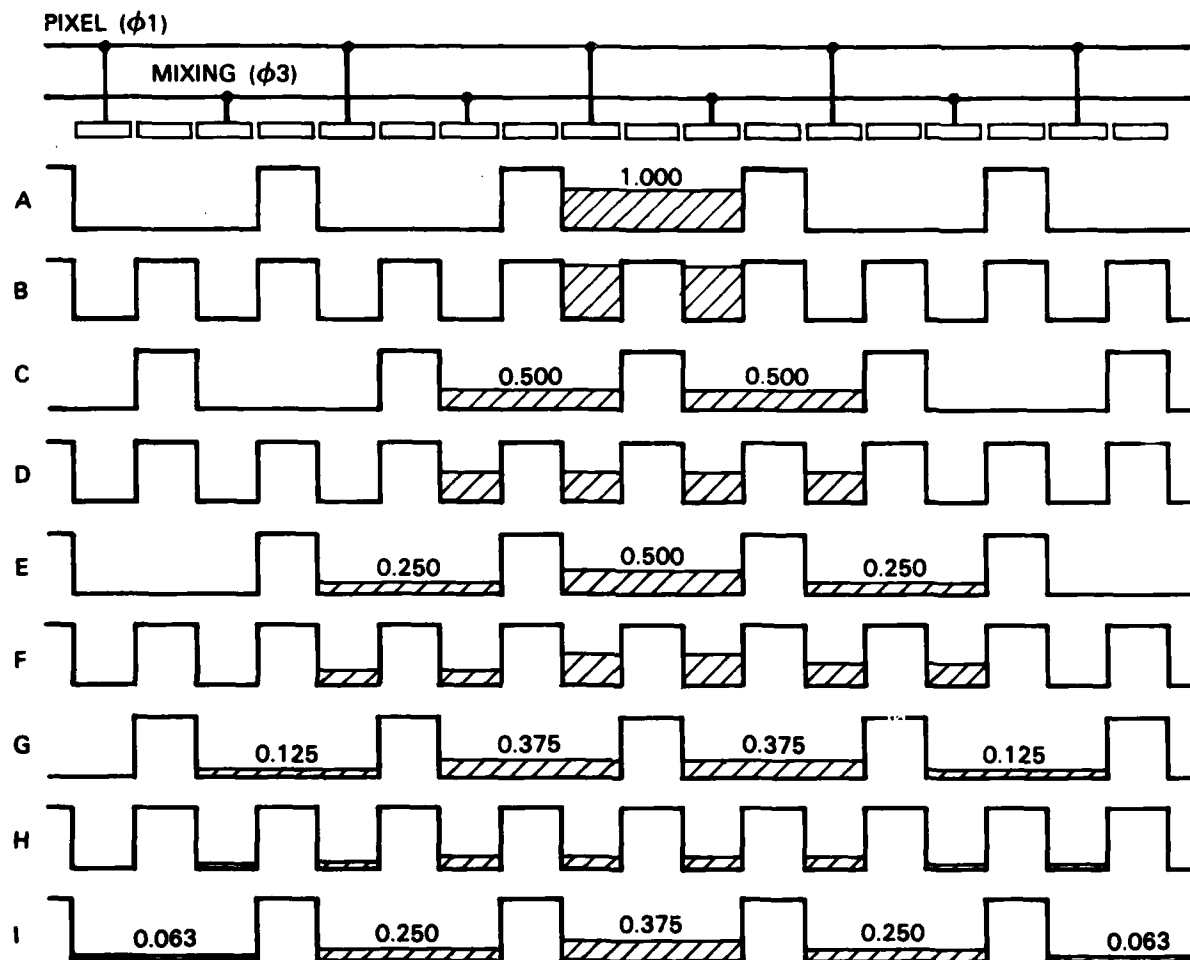


Figure 5-3. Potential wells and charge packets in a standard four-phase CCD clocked with the waveforms shown in Figure 5-2. Two mixing cycles are shown here.

TABLE 5-1

**Comparisons for 1, 2, 4, and 8 Mixing Cycles
of the Charge Packet Values Measured, the Values Expected
for an Idealized CCD, and the Values
for True Gaussian Convolution**

1 Mixing Cycle			2 Mixing Cycles		
Measured	Expected	True	Measured	Expected	True
0.75	0.750	0.760	0.95	0.937	0.933
0.25	0.250	0.260	0.70	0.687	0.691
			0.30	0.312	0.309
			0.08	0.062	0.067
8 Mixing Cycles			4 Mixing Cycles		
Measured	Expected	True	Measured	Expected	True
0.98	0.951	0.948	0.97	0.965	0.961
0.91	0.893	0.891	0.89	0.855	0.856
0.80	0.772	0.773	0.65	0.637	0.638
0.61	0.598	0.599	0.35	0.363	0.363
0.39	0.402	0.401	0.18	0.145	0.144
0.22	0.227	0.227	0.03	0.035	0.039
0.12	0.105	0.106			
0.04	0.038	0.040			



START



1 CYCLE



2 CYCLES



4 CYCLES



8 CYCLES



16 CYCLES

Figure 5-4. Photographs of the results obtained with a 32-stage four-phase CCD with 1, 2, 4, 8, and 16 mixing cycles applied to an initial pattern of eight full wells.

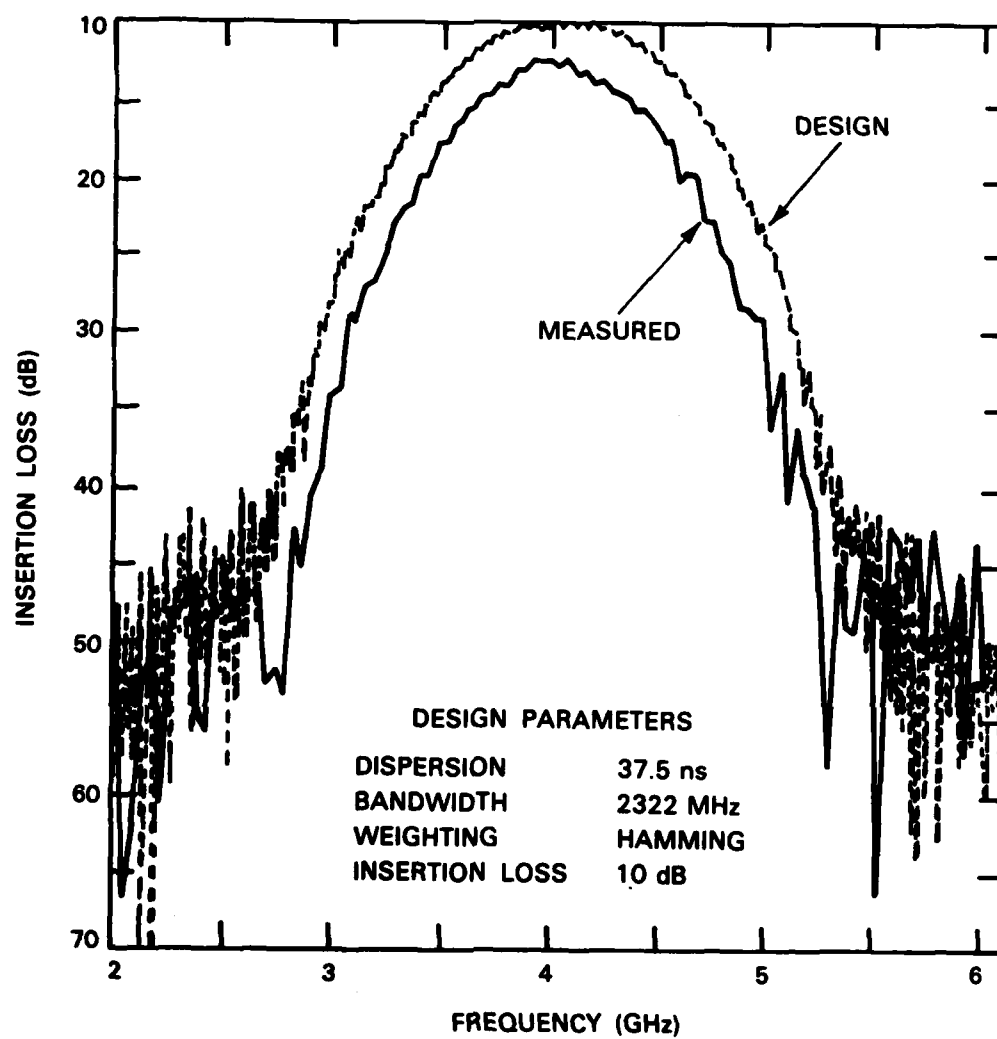


Figure 5-5. Insertion loss vs frequency of a Hamming-weighted superconductive chirp filter.

132216-N-01

expected values, and the values of a true Gaussian function for several mixing cycles. The expected approximation to a Gaussian function is extremely accurate after only a few mixing cycles. The measured and expected values have an rms deviation that corresponds to about 0.1 mm on the original photographs.

A future report will describe experiments now under way to produce two-dimensional Gaussian convolution of an image in a 576×384 -pixel CCD area imager of conventional design. Although this CCD has the serial-parallel-serial structure that uses only one-dimensional charge transfers in the main array, the complete two-dimensional Gaussian convolution can be performed within the imager in a fraction of the time required to clock the image out of the CCD. In a CCD area imager with two-dimensional charge transfer structures, the Gaussian convolution could be carried out in a few hundred microseconds or less.

J.P. Sage

5.2 SUPERCONDUCTIVE PULSE COMPRESSOR

Multigigahertz-bandwidth analog-signal-processing devices in the form of superconductive tapped electromagnetic delay lines have been realized,² pulse compression over a limited (800 MHz) bandwidth has been demonstrated,³ and trade-offs in the choice of dielectric substrates have been analyzed.^{4,5} Recently, the performance of an unweighted chirp filter with 35-ns dispersion and 2.6-GHz bandwidth was discussed.⁶ Here the performance of a matched pair of amplitude-weighted chirp filters in a pulse-compression system is described.

The tapped-delay-line structure consists of a cascade of backward-wave couplers, as described previously.⁶ Fabrication of these devices is as reported earlier,⁶ except that the superconducting niobium thin films are deposited on silicon, rather than sapphire, substrates. Silicon was chosen because it is a low-loss and isotropic dielectric at low temperatures.⁴ Both chirp filters are designed to have 37.5 ns of dispersion and a 2.3-GHz bandwidth (centered on 4 GHz) for a time-bandwidth product of 87. The strength of the backward-wave couplers is varied along the length of the devices to amplitude-weight the filter responses. One filter is designed to have a flat 10-dB insertion loss across the design bandwidth, while the other is weighted for a Hamming⁷ response with a 10-dB insertion loss at center frequency.

With the use of an automatic network analyzer, the CW phase and amplitude responses of the two filters were obtained from 2 to 6 GHz. The measured and predicted amplitude responses of the Hamming-weighted device are shown in Figure 5-5. The predictions were made with the first-principles theory used to design the device and are based on the physical design parameters of the device. Agreement between theory and experiment is excellent, although the device exhibits 2 or 3 dB more loss than predicted. Half of this loss is actually in the cryogenic probe, and the remainder could result from silicon substrates which are slightly thinner than the design value. Figure 5-6 shows the deviation of the measured phase from the best-fit quadratic. This best-fit quadratic implies a chirp slope within 0.5 percent of design. The remaining error has a rms value of 9.4° which, although much larger than the predicted error, is acceptable.

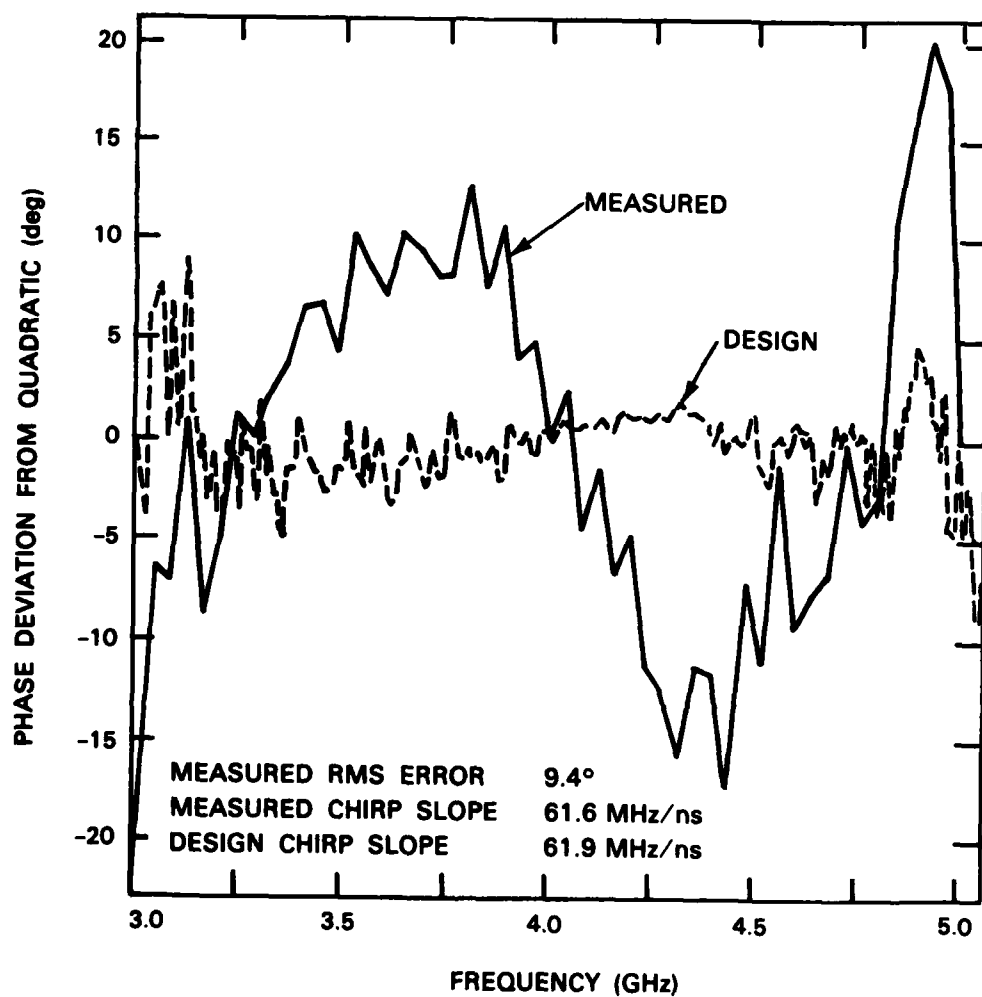


Figure 5-6. Phase error (deviation from quadratic) of a Hamming-weighted superconductive chirp filter.

The predicted and measured amplitude responses of the flat-weighted filter are shown in Figure 5-7. Again, agreement is excellent, even to the Fresnel ripple, which is strongest at the band edges. The test fixture accounts for most of the excess insertion loss. There is a slight upward shift in frequency of the device pass band. This is a result of a decrease in effective dielectric constant caused by a void between the two silicon wafers of the stripline structure. The measured phase shown in Figure 5-8 is, except for this frequency shift, in close agreement with theory. The best-fit quadratic implies a chirp slope almost 7 percent greater than the design value; this is also a consequence of the lowered dielectric constant.

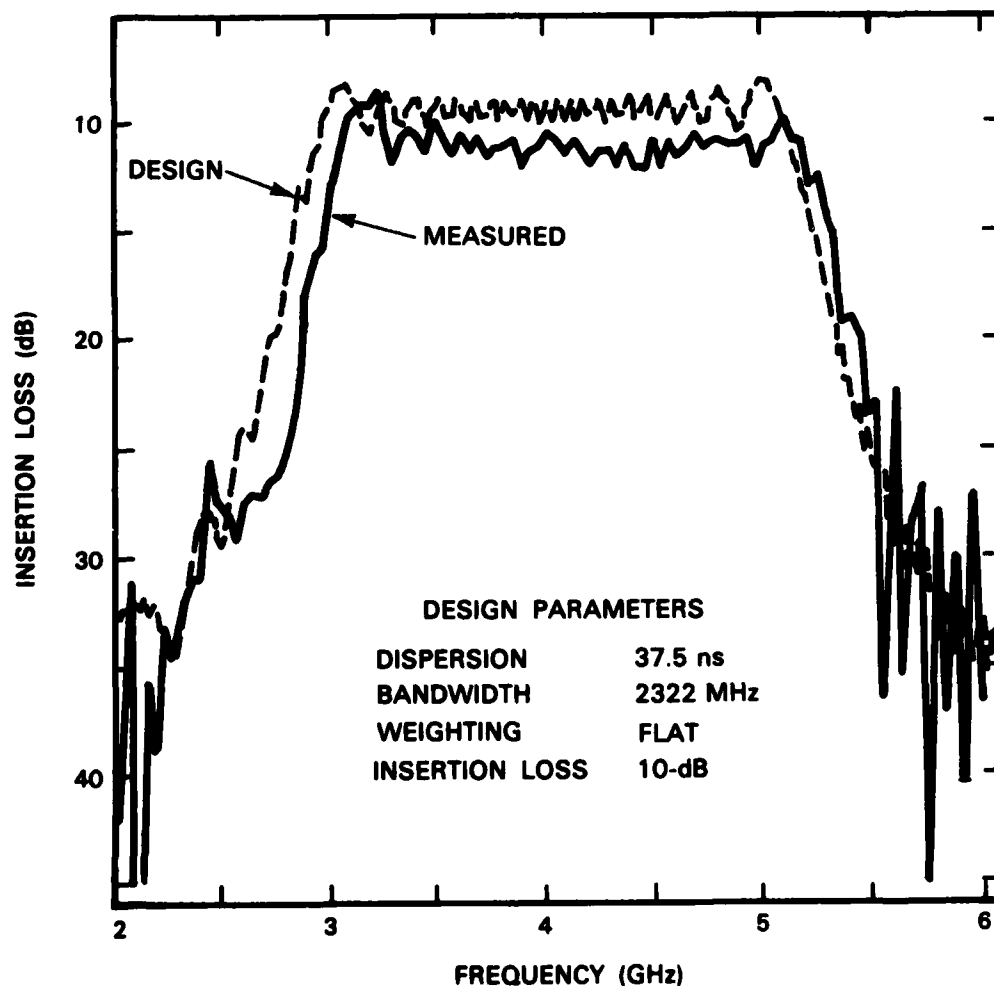


Figure 5-7. Insertion loss vs frequency of a flat-weighted superconductive chirp filter.

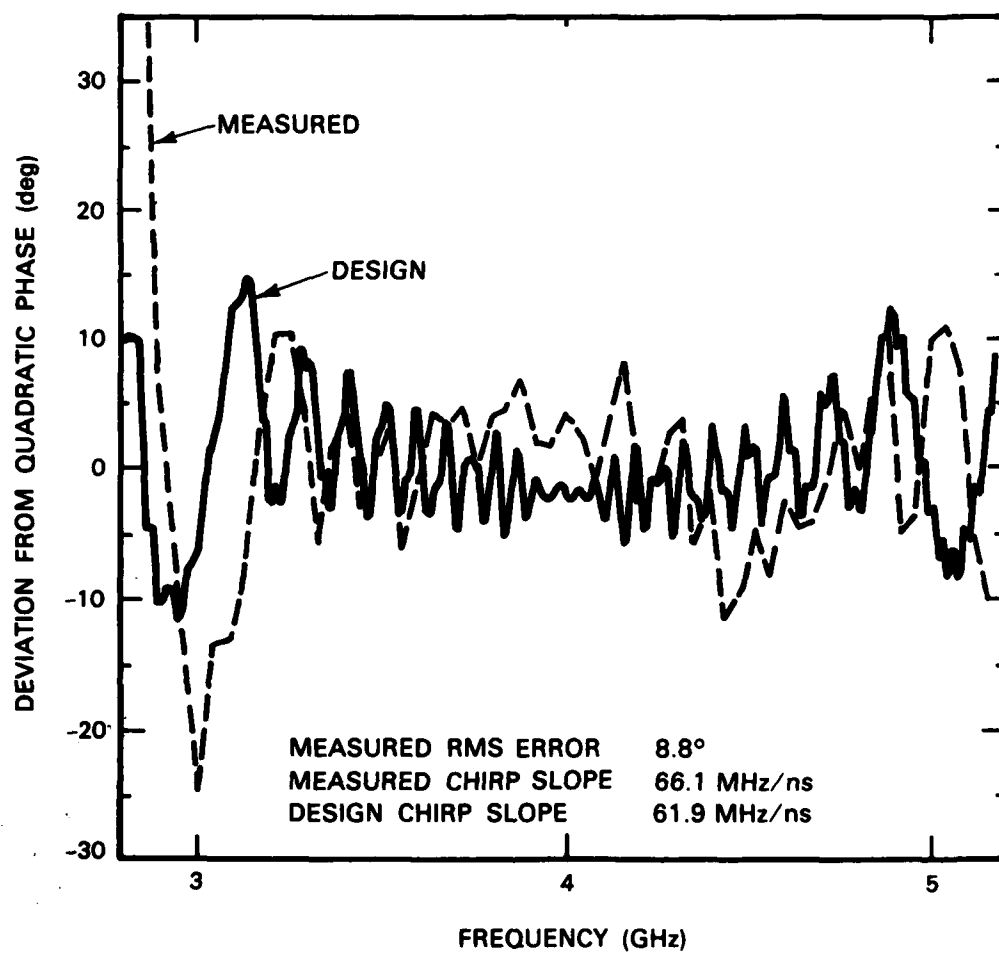


Figure 5-8. Phase error (deviation from quadratic) of a flat-weighted superconductive chirp filter.

132365-N-01

Using a 10-V video impulse of 135-ps width as input, the expanded up-chirp response of the Hamming-weighted filter was obtained. This was then applied directly to the down-chirp terminal pair of the flat-weighted filter. The resulting compressed-pulse response is shown in Figure 5-9(a). This pulse has a 4-dB full width of 0.7 ns, consistent with the 2.3-GHz bandwidth and Hamming weighting. Side lobes with a relative level of about -25 dB are evident in Figure 5-9(b). The predicted side lobe level of this device pair is -37 dB and should be reached by eliminating voids between the substrates and the variations in substrate thickness. The ideal -42-dB Hamming side lobes require a design with higher insertion loss or with phase predistortion⁸ to compensate for the effects of strong tapping and the consequent input wave depletion.

In summary, pulse compression over a 2.3-GHz bandwidth has been demonstrated with a matched pair of superconductive chirp filters. Device performance is respectable and deviations from ideal are understood; further performance improvements should follow from refinements in the mechanical aspects of device fabrication.

R.S. Withers

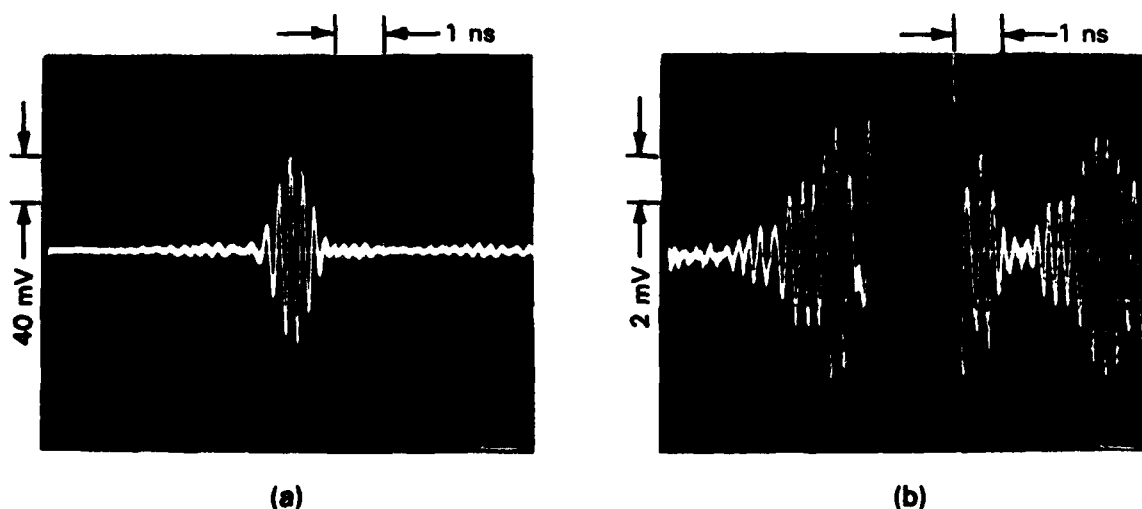


Figure 5-9. (a) Compressed pulse response of matched flat- and Hamming-weighted superconductive chirp filters and (b) same with 26 dB more gain.

REFERENCES

1. D. Marr and E. Hildreth, *Proc. Royal Soc. London* **B207**, 187 (1980).
2. Solid State Research Report, Lincoln Laboratory, M.I.T. (1981:2), p. 57, DTIC AD-A110947/9.
3. *Ibid.* (1982:2), p. 89, DTIC AD-A122252.
4. *Ibid.* (1982:3), p. 74, DTIC AD-A124305/4.
5. *Ibid.* (1983:2), p. 55, DTIC AD-A134594.
6. *Ibid.* (1983:1), p. 83, DTIC AD-A128894/3.
7. C. E. Cook and M. Bernfeld, *Radar Signals* (Academic Press, New York, 1967), p. 182.
8. R.S. Withers and P.V. Wright, *Proc. 7th Annual Frequency Control Symposium* (IEEE, New York, 1983), p. 81.

UNCLASSIFIED

SECURITY CLASSIFICATION OF THIS PAGE (When Data Entered)

REPORT DOCUMENTATION PAGE		READ INSTRUCTIONS BEFORE COMPLETING FORM
1. REPORT NUMBER ESD-TR-83-223	2. GOVT ACCESSION NO. AD-A142991	3. RECIPIENT'S CATALOG NUMBER
4. TITLE (and Subtitle) Solid State Research		5. TYPE OF REPORT & PERIOD COVERED Quarterly Technical Report 1 August — 31 October 1983
7. AUTHOR(s) Alan L. McWhorter		6. PERFORMING ORG. REPORT NUMBER 1983:4
9. PERFORMING ORGANIZATION NAME AND ADDRESS Lincoln Laboratory, M.I.T. P.O. Box 73 Lexington, MA 02173-0073		8. CONTRACT OR GRANT NUMBER(s) F19628-80-C-0002
11. CONTROLLING OFFICE NAME AND ADDRESS Air Force Systems Command, USAF Andrews AFB Washington, DC 20331		10. PROGRAM ELEMENT, PROJECT, TASK AREA & WORK UNIT NUMBERS Program Element No. 63250F Project No. 649L
14. MONITORING AGENCY NAME & ADDRESS (if different from Controlling Office) Electronic Systems Division Hanscom AFB, MA 01731		12. REPORT DATE 15 November 1983
		13. NUMBER OF PAGES 88
		15. SECURITY CLASS. (of this report) Unclassified
		16a. DECLASSIFICATION DOWNGRADING SCHEDULE
18. DISTRIBUTION STATEMENT (of this Report) Approved for public release; distribution unlimited.		
17. DISTRIBUTION STATEMENT (of the abstract entered in Block 20, if different from Report)		
19. SUPPLEMENTARY NOTES None		
20. KEY WORDS (Continue on reverse side if necessary and identify by block number)		
solid state devices	photodiode devices	infrared imaging
quantum electronics	lasers	surface-wave transducers
materials research	laser spectroscopy	charge-coupled devices
microelectronics	imaging arrays	acoustoelectric devices
analog device technology	signal processing	
20. ABSTRACT (Continue on reverse side if necessary and identify by block number)		
<p>This report covers in detail the solid state research work of the Solid State Division at Lincoln Laboratory for the period 1 August through 31 October 1983. The topics covered are Solid State Device Research, Quantum Electronics, Materials Research, Microelectronics, and Analog Device Technology. Funding is primarily provided by the Air Force, with additional support provided by the Army, DARPA, Navy, NASA, and DOE.</p>		

DD FORM 1473 EDITION OF 1 NOV 66 IS OBSOLETE
1 Jan 73

UNCLASSIFIED

SECURITY CLASSIFICATION OF THIS PAGE (When Data Entered)

END

FILMED

8

11

10/10